NINJ1 mediated plasma membrane rupture is a two-step process requiring cell swelling

Ella Hartenian[1†], Elliott M. Bernard[1†], Giulia Ammirati[2], Hubert B. Leloup[3], Magalie Agustoni[1], Lukas Bissegger[4], José Carlos Santos[1], Ivo Glück[5], Stefania A. Mari[2], Christian Sieben[5], Virginie Petrilli[3], Sylvain Monnier[6], Daniel J. Müller[2] and Petr Broz[1*]

1. Department of Immunobiology, University of Lausanne, Epalinges, Switzerland
2. Department of Biosystems Science and Engineering, ETH Zurich, Basel, Switzerland
3. Centre de Recherche en Cancérologie de Lyon INSERM U1052-CNRS UMR5286, Université Claude Bernard, Lyon, France
4. Department of Biomedicine, University of Basel, Basel, Switzerland
5. Nanoscale Infection Biology Group, Helmholtz Centre for Infection Research and Institute for Genetics, Technische Universität Braunschweig, Braunschweig, Germany
6. Université de Lyon, Université Claude Bernard Lyon 1, CNRS, Institut Lumière Matière, F-69622, Villeurbanne, France

† These authors contributed equally
Correspondence: pbroz@unil.ch

Key words
Cell death; NINJ1; ferroptosis; PMR; inflammation; necrosis

Abstract
Plasma membrane rupture and the release of cytosolic contents are hallmarks of necrotic cell death. The plasma membrane protein ninjurin-1 (NINJ1) actively promotes cell lysis by polymerizing into membrane embedded filaments that induce the formation of large plasma membrane lesions. Yet the signals controlling NINJ1 oligomerization and lesion opening remain unknown. Here, we combine cell biology and biophysical measurements to characterize the steps preceding NINJ1-induced PMR. Our results show that NINJ1 lesions form through a 2-step mechanism requiring oligomerization, which is triggered by signal 1, and subsequent lesion opening driven by signal 2, which we determine to be cell swelling without a concomitant increase in intracellular pressure. The close homolog NINJ2 oligomerizes with similar kinetics to NINJ1 but fails to form lesions during cell swelling. NINJ1-NINJ2 chimeras identify that the unstructured N-terminal region of NINJ1 controls lesion opening. In summary, our data establish a 2-step model for NINJ1-driven necrosis.

Introduction

A timely, proportionate and correctly localized inflammatory response during tissue damage and infection requires the release of cytokines, chemokines and damage-associated molecular patterns (DAMPs), which recruit and activate immune cells to eliminate pathogens, clear debris and initiate healing[1]. Meanwhile, aberrant release of DAMPs can contribute to autoinflammatory disease[2]. An important source of these molecules is dying cells, especially those undergoing necrotic forms of cell death such as necroptosis, pyroptosis and ferroptosis. Apoptosis, classically thought of as an immunologically "silent" form of cell death, can also become a source of DAMPs when the number of apoptotic corpses overwhelms their removal by phagocytes (efferocytosis), resulting in secondary necrosis and inflammation[3].

Pyroptosis and necroptosis are initiated by effector proteins, gasdermins (GSDMs) and mixed lineage kinase domain like pseudokinase (MLKL) respectively, that form pores in the plasma membrane[4]. Whilst MLKL pores have only been shown to allow the movement of cations[5], the GSDMD pore, with an inner diameter of approximately 22 nm, can permit the secretion of certain cytokines, including IL-1β and IL-18, low molecular weight proteins such as S100A8/S100A9, as well as oxylipins[6–8]. However, the relatively small size of these pores is unable to explain the release of larger DAMPs, including HMGB1 and nuclear proteins, that is associated with necrotic forms of cell death. Thus, for many years, DAMP release has been attributed to osmotic pressure buildup, followed by cell swelling and eventual passive plasma membrane rupture (PMR), all of which are classical hallmarks of cell necrosis.

In a seminal paper in 2021, Kayagaki *et al.* demonstrated that ninjurin-1 (NINJ1) is essential for plasma membrane rupture and the release of DAMPs during pyroptosis and even secondary necrosis of apoptotic cells[9]. It has subsequently been confirmed that NINJ1 is also important for plasma membrane rupture during a range of cell death modalities, including ferroptosis, cuproptosis, and death induced by pore forming toxins[10,11]. NINJ1 is a 16 kDa plasma membrane resident protein that is highly conserved in mammals and is widely expressed in various tissues and cell types. At resting state NINJ1 has 3 straight transmembrane helices (TM1-3) and forms a face-to-face autoinhibited homodimer through interactions between the hydrophilic faces of each monomer[12]. During cell death the homodimer dissociates, allowing monomeric NINJ1 to oligomerize into fence-like filaments of up to several hundred nanometers in length[13–15]. During this oligomerization step, TM1 undergoes an almost 90-degree kink to form the short helices α1 and α2, of which α1 connects neighboring protomers, thereby stabilizing the filament. How cell death triggers the dissociation of NINJ1 homodimers, its subsequent oligomerization and plasma membrane rupture remain open questions.

The fact that necrotic cells release large DAMPs in a NINJ1-dependent manner suggests that oligomeric NINJ1 causes the formation of large plasma membrane lesions, however, how NINJ1 filaments form these lesions remains to be experimentally confirmed. Given the amphipathic nature of NINJ1 filaments several non-mutually exclusive models have been proposed. One possibility is that individual filaments form pores by capping membrane edges through their hydrophobic face, while forming a channel by their hydrophilic face, similar to the pore formation mechanism proposed for GSDMD and other pores[16]. Alternatively, it is possible that NINJ1 forms a double filament in the plasma membrane by association of the hydrophilic faces of each filament, and that the opening of such a double-filament zipper provides a hydrophilic conduit through which DAMPs can exit the cell[14]. Based on the observation that recombinant NINJ1 filaments tend to curve and expose the hydrophilic face on their convex side, a third model suggests that circular NINJ1 filaments can solubilize discs of plasma membrane lipids ('cookie-cutter' model)[15]. It remains unclear if one or all three of these models are correct, and how a double filament NINJ1 zipper could be opened is unknown. However, all three models require the opening of NINJ1 lesions in the cell membrane.

In this manuscript we investigate the activation mechanism of NINJ1 and demonstrate for the first time that NINJ1 oligomerization and NINJ1-dependent PMR are two distinct events that can be experimentally separated. We focus on ferroptosis to interrogate the upstream events prior to NINJ1-mediated plasma membrane rupture and identify oligomeric NINJ1 that has not yet ruptured the plasma membrane. We demonstrate that osmotic swelling of cells is critical to endow such NINJ1 oligomers with membrane-rupturing properties, as experimental inhibition of cell swelling abrogates cell lysis but not NINJ1 oligomerization. We then use atomic force microscopy to measure the pressure in dying cells, which shows that cell swelling correlates with a slow expansion at constant hydrostatic pressure that dissipates once NINJ1 perforates the membrane, dispelling the long-hold belief that necrotic cell swelling is caused by an increase in internal pressure. Since cell swelling causes tensile stress on the plasma membrane[17,18], these data suggest that NINJ1 lesions open in response to mechanical stress caused by the expanding plasma membrane. Finally, we define the NINJ1 N-terminal domain as the region that mediates the transition from inactive to active oligomers by creating a series of chimeras between NINJ1 and NINJ2, a homolog that oligomerizes into filaments during death, but fails to efficiently permeabilize the plasma membrane. Overall, we propose a two-step model for NINJ1-driven necrosis, in which NINJ1 oligomerizes to form inactive plasma membrane-embedded filaments that serve as weak points in the membrane and that lead to the formation of lesions that open once the cell swells.

Results

Ferroptotic cell swelling coincides with NINJ1-mediated plasma membrane rupture

NINJ1 activation must follow a conserved event that occurs in necrotic forms of cell death, such as pyroptosis, secondary necrosis and ferroptosis. We thus hypothesized that such an event would precede NINJ1 activation and occur independently of NINJ1, and that blocking it would prevent NINJ1 activation. To identify this event we focused on ferroptosis, in which NINJ1-driven PMR follows lipid peroxidation, ion fluxes and cell swelling[10,11], and tried to pinpoint when NINJ1 is activated. In murine bone marrow derived macrophages (BMDMs) treated with the ferroptosis trigger ML162, a GPX-4 inhibitor, we observed that NINJ1-dependent uptake of propidium iodide (PI) began around 2.5 hours (h) post treatment (**Figure 1A**), which was shortly followed by NINJ1-dependent LDH release at 3 h post treatment (**Figure 1B**). NINJ1-dependent PI uptake and cell lysis correlated with NINJ1 oligomerization as detected by crosslinking immunoblots (**Figure 1C**). Similar analyses in mouse embryonic fibroblasts (MEFs) showed that NINJ1-dependent PI uptake began between 3 and 4 h post treatment with the first detectable LDH release observed at 5 h (**Figure S1A&B**). NINJ1 oligomerization was first observed on crosslinking immunoblots at 4 h post treatment and increased over time (**Figure S1C**). Overall, these results suggest that NINJ1 activation during ferroptosis is marked by a rapid loss of membrane integrity, detectable as an uptake of small (~700 Da) DNA binding dyes, before oligomerization and LDH release can be observed.

Calcium influx and cell swelling have been reported to be among the first hallmarks of lytic cell death[19]; we thus tested how these relate to NINJ1-dependent loss of membrane integrity. In BMDMs, cytosolic Ca^{2+} concentrations increased within 60-90 minutes (min) post ferroptosis induction and clearly preceded PI uptake (**Figure S1D&E**), indicating that the opening of small ion channels or the formation of lipid micro-lesions occurs before NINJ1 activation. Moreover, Ca^{2+} influx proceeded with comparable kinetics in both WT and *Ninj1*$^{-/-}$ cells, which prompted us to investigate if Ca^{2+} provides the signal that causes NINJ1 activation.

To test if Ca^{2+} influx alone is sufficient to activate NINJ1 we treated WT and *Ninj1*$^{-/-}$ BMDMs with ionomycin, an ionophore that induces Ca^{2+} influx into cells, and monitored NINJ1 oligomerization and LDH release. We observed rapid NINJ1 oligomerization and NINJ1-dependent LDH release after ionomycin treatment, which did not occur in the absence of extracellular Ca^{2+} (**Figure S1F-H**), in agreement with a recent preprint[20]. However, cell viability measurements of intracellular ATP showed a decrease in both WT and *Ninj1*$^{-/-}$ macrophages, demonstrating that ionomycin induces cell death in a NINJ1-independent manner (**Figure S1I**). We attempted to define if cell death was occurring through a known programmed cell death pathway, however immunoblotting of ionomycin treated WT BMDMs failed to show any

hallmarks of pyroptosis (Caspase-1 and GSDMD cleavage), apoptosis (Caspase-3 cleavage), or necroptosis (MLKL phosphorylation), while cells undergoing each of these cell death pathways displayed the expected hallmarks (**Figure S1J**). In addition, we measured LDH release from ionomycin treated *Caspase1/11*$^{-/-}$ and *Ripk3*$^{-/-}$ BMDMs, which was unchanged, further confirming that cell death was not occurring through pyroptosis or necroptosis (**Figure S1K**). Finally, we ruled out ferroptosis as the cause of ionomycin-induced cell death as the inhibitor ferrostatin-1 (Fer-1) did not block ionomycin-induced LDH release, while efficiently blocking ML162-induced cell lysis (**Figure S1L**). Thus Ca^{2+} influx by ionomycin induces NINJ1 activation as well as a rapid metabolic death of macrophages that proceeds independently of known regulated cell death pathways. Whether this death triggers NINJ1 activation upon ionomycin treatment, or if ionomycin-induced Ca^{2+} influx directly triggers NINJ1 activation and in parallel metabolic death remains to be shown.

As ionomycin-induced Ca^{2+} influx led to rapid NINJ1 oligomerization that could be abrogated by calcium free medium, we next tested if Ca^{2+} influx via small channels/lesions drove NINJ1 activation during ferroptosis. To this end, we induced ferroptosis in calcium-free media and measured LDH release. We observed similar levels of cell lysis in the presence and absence of extracellular calcium (**Figure S1M**) indicating that Ca^{2+} uptake was not required for NINJ1 activation in this context. Thus, while Ca^{2+} uptake is sufficient to trigger NINJ1 oligomerization upon ionomycin treatment, it does not seem to play a role in NINJ1 activation upon ferroptosis induction and another signal is thus needed. Finally, we asked if the mechano-gated ion channels PIEZO1 and 2 could lead to NINJ1 activation during ferroptosis due to an influx of cations[21,22]. We induced ferroptosis in PIEZO1/2-deficient (*Piezo1*$^{fl/fl}$*Piezo2*$^{fl/fl}$*LysM-Cre*) BMDMs[23] and observed no difference in LDH release or NINJ1 crosslinking as compared to WT controls (**Figure S1N&O)**. Thus, neither chemical nor genetic means of blocking Ca^{2+} influx affected NINJ1-mediated PMR during ferroptosis.

While performing Ca^{2+} imaging, we noticed that ferroptotic cells begin to swell after calcium influx and prior to timepoints where NINJ1 was activated, as determined by PI uptake (**Figure S1D**). To define the temporal correlation between swelling and NINJ1 activation we next performed live cell imaging of WT and *Ninj1*$^{-/-}$ BMDMs undergoing ferroptosis in the presence of the membrane impermeable DNA-binding dye DRAQ7 and the membrane stain CellBrite. This allowed us to determine the diameter of the cells over time and thus to measure changes in cell size[24]. Both WT and *Ninj1*$^{-/-}$ BMDMs showed the first signs of size increase, normalized to their initial size in the first frame of imaging, about 60 min prior to NINJ1 activation, determined by a rapid increase in DRAQ7 uptake (**Figure 1D-F, Figure S2A&B, Movie 1&2**). The first detectable entrance of DRAQ7 into the nucleus was set as time 0. Cells of both

genotypes swelled to 160% of their initial diameter prior to DRAQ7 uptake. Consistent with PI measurements (**Figure 1A**), the uptake of DRAQ7 was more rapid in WT macrophages than in *Ninj1*$^{-/-}$ macrophages (**Figure 1E&F**).

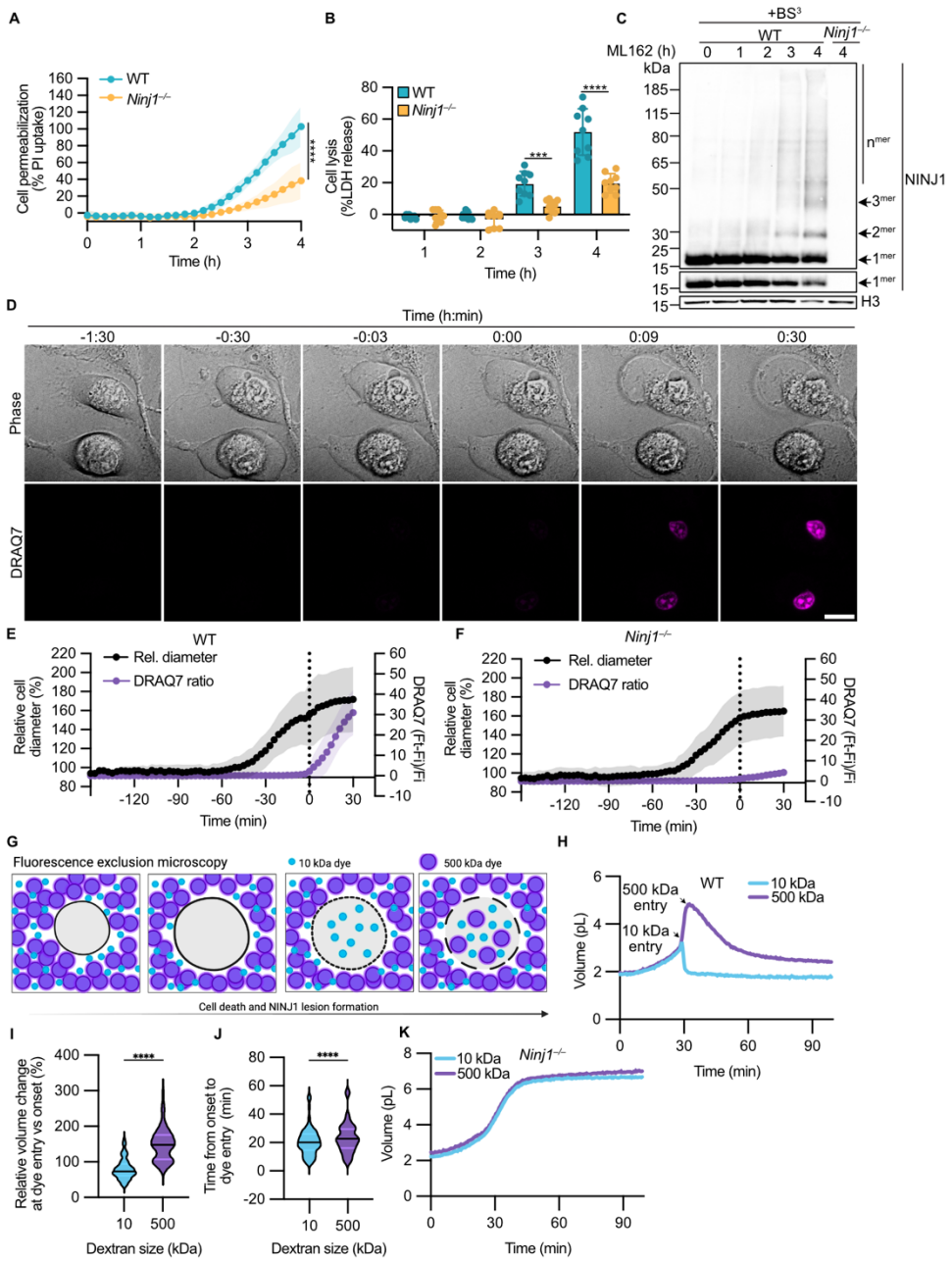

Figure 1 Cell swelling coincides with NINJ1-mediated plasma membrane rupture. A-C WT and *Ninj1*$^{-/-}$ BMDMs were stimulated with ML162 for indicated time points and analyzed for PI uptake every 10 minutes (**A**), LDH release (**B**), and NINJ1 oligomerization by crosslinking immunoblot (**C**), H3 serves as a loading control. **D** Stills from live cell imaging of WT BMDMs stimulated with ML162 in the presence of DRAQ7. Scale bar 10 µm. **E-F** Quantification of the diameter of WT (**E**) and *Ninj1*$^{-/-}$ (**F**) BMDMs undergoing ferroptosis and corresponding DRAQ7 ratios. **G** Schematic representation of fluorescence exclusion microscopy approach used to measure cell volume and lesion size. **H** Volume measurements in picoLiters (pL) using FXm of WT iBMDMs treated with cumene hydroperoxide (CuOOH) in the presence of small (10 kDa Alexa647 Dextran) and large (500 kDa FITC Dextran) dyes. Time 0 indicates the onset of swelling. **I** Quantification of the relative change in cell volume of WT iBMDMs treated with CuOOH from onset of swelling to the uptake of 10 kDa and 500 kDa dextrans. **J** Quantification of the time between the onset of swelling and uptake of 10 kDa and 500 kDa dextrans by WT iBMDMs treated with

CuOOH as measured by FXm. **K** Volume measurements in picoLiters (pL) using FXm of *Ninj1*$^{-/-}$ iBMDMs treated with CuOOH in the presence of small (10 kDa) and large (500 kDa) dextrans. Data in A and B are mean ± SD from 3 independent experiments. Western blot in C and images in D are representative of 3 independent experiments. Data in E and F are mean ± SD of 20 cells from 3 independent experiments. Data in H&K are from 1 cell, representative of at least 30 cells measured in 2 independent experiments. Data in I and J are from 60 cells from 2 independent experiments. Data in A and B were analyzed by 2-way ANOVA followed by Šídák's multiple comparisons tests. ns not significant, *** $p<0.001$, **** $p<0.0001$. Data in I and J were analyzed by two-tailed Wilcoxon matched-pairs signed rank test.

Thus, our results reveal context-dependent roles for Ca^{2+} influx in NINJ1-dependent PMR. While cytosolic Ca^{2+} influx is not required for NINJ1 activation during ferroptosis, it is essential for ionomycin induced NINJ1 oligomerization and NINJ1-dependent PMR. If, in the latter context, Ca^{2+} influx directly activates NINJ1, or via induction of cytotoxicity remains to be determined. On the other hand, cell swelling correlates with NINJ1-mediated PMR.

Increases in cell volume correlate with a gradual opening of NINJ1 lesions

To more precisely measure cell swelling during ferroptosis, we next utilized a technique based on fluorescence exclusion microscopy (FXm) that can measure cell volume changes over time, and that was recently used to follow the swelling of pyroptotic cells[25]. In brief, cells are grown in a microfluidic chamber of defined height in the presence of small (10 kDa) and large (500 kDa) membrane impermeable dextrans coupled to fluorescent dyes, and cell volume is estimated by the exclusion of the fluorescent signal (**Figure 1G**). Entry of the dyes into the cell can additionally be used to precisely determine the time point of membrane permeabilization and estimate the size of membrane lesions. These measurements demonstrated that during ferroptosis the volume of WT immortalized BMDMs (iBMDMs) increases before the entry of the 10 kDa dye, indicative of initial pore formation, which is then followed minutes later by uptake of the 500 kDa dye (**Figure 1H-J, Figure S2C&D**). Importantly, in the minutes between the uptake of the small and large dye there is a further increase in cell volume. The short temporal delay between the uptake of the two dyes could either indicate a gradual growth of NINJ1 lesions by progressive NINJ1 oligomerization, or two states of NINJ1 lesions, e.g. a partially closed and a fully open state. Interestingly, we did not observe any uptake of the dyes in *Ninj1*$^{-/-}$ iBMDMs and the cells remained swollen until the end of the experiment (**Figure 1K, Figure S2E&F**), corroborating previous findings that in macrophages NINJ1 is the only ferroptotic pore[10]. Finally, we confirmed that the volume of vehicle (ethanol) treated WT iBMDMs did not change over a 90 min timecourse (**Figure S2G**).

These results thus describe with unprecedented accuracy the formation of NINJ1-dependent lesions in the membrane of WT macrophages that occurs shortly (within 30-60 min) after cells start to swell. Furthermore, the findings indicate NINJ1 lesions can exist as smaller and larger membrane pores, correlating with the volume of the cell.

Swelling drives the opening of NINJ1 lesions

Given that swelling precedes the formation of NINJ1 lesions and is a hallmark of all forms of necrosis[24,25], we next aimed to test if swelling could act as the universal signal that activates NINJ1. Swelling can be experimentally reduced by the addition of hydrophilic molecules, such as large polyethylene glycols (PEGs) or sucrose, to the cell culture medium to reduce the difference in osmolarity between the outside and inside of the cell. We thus first measured the cell diameter and DRAQ7 uptake in WT BMDMs undergoing ferroptosis in the presence of large PEGs. In the presence of 10 mM PEG6000 (310 mOsm) ferroptotic cells swelled slightly, to approximately 120% of their initial diameter, before collapsing, acquiring DRAQ7 signal and shrinking to 80% of their initial diameter (**Figure 2A&B, Figure S3A, Movie 3**). In comparison, ferroptotic cells in regular OptiMEM (265 mOsm) swelled to 160% of their initial diameter and this swelling was maintained even after DRAQ7 influx (**Figure 1D&E**).

Having validated that PEG6000 could efficiently block cell swelling, we next tested its impact on PI uptake (measuring membrane integrity) and LDH release (measuring cell lysis) and found that while PEG6000 only partially reduced PI uptake, it robustly reduced cell lysis (**Figure 2C&D**). Smaller PEGs had a similar effect on swelling, PI uptake and LDH release, even though higher concentrations were necessary to achieve inhibition (**Figure 2C-E**). Importantly, while PEGs prevented cell swelling and PMR, they did not block ferroptotic death, as confirmed by a loss of cellular ATP in PEG and ML162 treated cells (**Figure S3B**). A similar inhibition of PMR was observed in ferroptotic MEFs treated with PEGs (**Figure S3C**). To corroborate the PEG data, we also tested another osmolyte, sucrose. In agreement with the PEGs, sucrose concentrations of 250 mM (470 mOsm) and above impaired swelling and reduced LDH release from ferroptotic BMDMs (**Figure S3D&E**) and MEFs (**Figure S3F**). In summary these findings showed that swelling is an important prerequisite for NINJ1-dependent PMR.

To further define how inhibition of cell swelling prevented NINJ1-dependent PMR, we next tested if PEGs or sucrose abrogated the formation of NINJ1 filaments, in a manner akin to glycine which blocks LDH release by preventing NINJ1 oligomerization[26]. Unexpectedly, we found NINJ1 oligomerization during ferroptosis was largely unaffected by the presence of PEG600, PEG6000 or sucrose at concentrations that prevented LDH release (**Figure 2F & Figure S3G**). Only in the presence of 200 mM PEG600 did we observe a small reduction in the amount of NINJ1 oligomerization. Importantly, the tested concentrations of osmolytes alone did not cause any NINJ1 oligomerization, excluding PEGs and sucrose as direct activators of NINJ1 (**Figure 2F & Figure S3G**). In summary, these findings indicate that

swelling is not essential for the formation of NINJ1 oligomers, but solely required for their functionalization and the opening of membrane lesions.

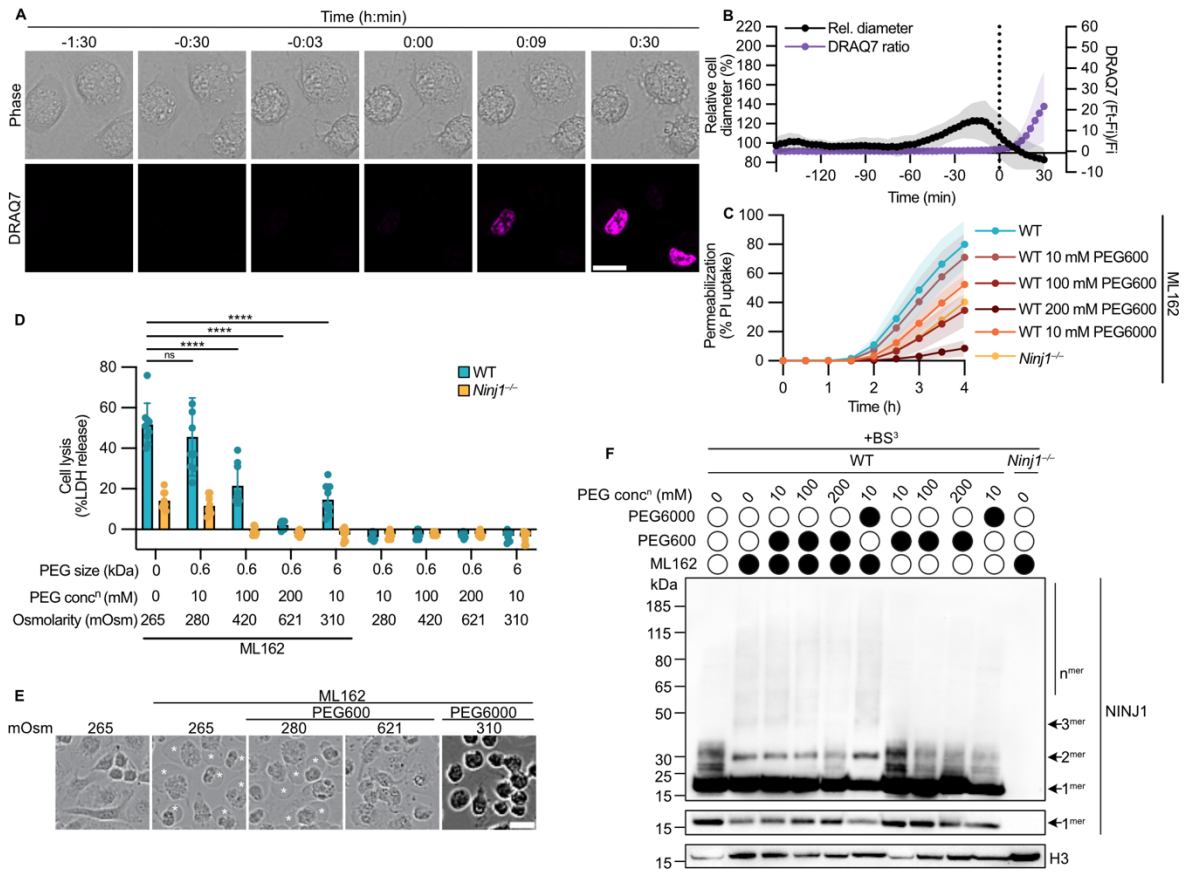

Figure 2 Lesion formation by NINJ1 oligomers requires osmotic swelling. A Stills from live cell imaging of WT BMDMs stimulated with ML162 in the presence of 10 mM PEG6000 and DRAQ7. Scale bar 10 µm. **B** Quantification of the diameter of BMDMs undergoing ferroptosis and corresponding DRAQ7 ratios in the presence of 10 mM PEG6000. **C-D** WT and *Ninj1*$^{-/-}$ BMDMs were stimulated with ML162 in media containing the indicated concentrations of PEG600 or PEG6000 and PI uptake (**C**) and LDH release at 4 h (**D**) analyzed. **E** Phase contrast images from an Incucyte of WT BMDMs stimulated or not with ML162 for 4 h in the presence of the indicated osmolarities of PEG600 and PEG6000. Asterisks indicate balloons. Scale bar 20 µm. **F** Crosslinking immunoblot analysis of NINJ1 in WT and *Ninj1*$^{-/-}$ BMDMs following stimulation with ML162 and the indicated concentrations of PEG600 and PEG6000 for 4 h. Images in A and E and Western blot in F are representative of 3 independent experiments. Data in B are mean ± SD of 20 cells from 3 independent experiments. Data in C and D are mean ± SD from 3 independent experiments. Data in D were analyzed by 2-way ANOVA followed by Šídák's multiple comparisons tests, ns not significant, **** $p<0.0001$.

In agreement with NINJ1 oligomerization preceding lesion formation, live cell imaging of HeLa cells undergoing ferroptosis revealed that following NINJ1 oligomerization, as measured through inhomogeneity analysis[14], there is a delay of approximately 20 minutes before DRAQ7 uptake was detected (**Figure S3H**). Thus, NINJ1 oligomerization and NINJ1-mediated PMR occur as temporally separable events.

We next subjected BMDMs to hypotonic buffers to assess if swelling alone was sufficient to induce NINJ1-dependent plasma membrane rupture. We observed some NINJ1 oligomerization but no NINJ1-dependent LDH release with the lowest osmolarity (76 mOsm) (**Figure S4A-B**). If cell swelling acts as a direct trigger of NINJ1 under these conditions, we would expect NINJ1-deficiency to prevent the death of cells in hypotonic media. We thus measured cell viability of both WT and *Ninj1*$^{-/-}$ BMDMs by determining the levels of cellular ATP but found that both genotypes lost ATP to a similar extent (**Figure S4C**). It is therefore unlikely that NINJ1 responds to cell swelling alone under hypotonic conditions.

Overall, these results suggest that NINJ1-driven PMR is executed in two steps: a yet-to-be-defined trigger first initiates the oligomerization of NINJ1 into filaments that remain inactive and, based on the data presented here, cell swelling is the second signal that activates NINJ1 filaments to form membrane lesions.

Intracellular pressure does not increase during ferroptosis

Membrane blebbing and cell swelling during necrosis are assumed to be caused by water influx and a rise in osmotic pressure within cells that forces the plasma membrane to expand[27]. To determine if an increase in intracellular pressure could explain the observed increase in cell volume and drive NINJ1-mediated plasma membrane rupture, we measured intracellular pressure using atomic force microscopy (AFM). Here, a micrometer sized bead attached to a cantilever is used to indent cells and the force required to make a 500nm indentation is used to calculate the intracellular pressure (**Figure 3A**). Both outward-directed hydrostatic (osmotic) pressure and the inward-directed counterforce of the actomyosin cortex[28] contribute to intracellular pressure. We first recorded the pressure in WT MEFs undergoing ML162-induced death every 30 min, classifying the cells by their morphology. We observed a striking decrease in cellular pressure in the first 30 min after addition of ML162, which corresponded with cells transitioning from a flat, spread morphology to a rounded one (**Figure 3B**). The decrease in pressure continued until 1.5 h post ML162 addition, after which a period of low but constant pressure was reached and cells started to adopt a swollen, blebbing morphology. Thus, these analyses define a rounding phase with a drop in internal pressure, and a swelling phase in which the lower cell pressure stays constant. Interestingly, at the end of the swelling phase, WT cells lose membrane integrity and acquire PI staining (**Fig. 3B**).

To understand if the early decrease in pressure was NINJ1-dependent, we repeated the measurements in WT cells treated with glycine, a known inhibitor of NINJ1 oligomerization and PMR[26,29]. We again saw an initial steep decline in pressure after ML162 addition that was independent of the presence or absence of glycine (**Figure 3C**). Monitoring the cells during

the swelling and permeabilization phases, *i.e.* from 3 to 7 h post ML162 addition, showed that glycine addition prevented a 2nd loss of pressure that occurred in WT cells, and even resulted in a rise in internal pressure towards the end of the experiment. To further confirm if these events were truly NINJ1 dependent, we next measured pressure in WT and *Ninj1* KO MEFs following ML162 treatment. At early time points post ML162 addition we measured no significant pressure difference in WT compared to *Ninj1* KO MEFs, confirming the data acquired with glycine treated cells. Furthermore, we observed that the second pressure drop was NINJ1-dependent as only WT but not *Ninj*1 KO cells experienced a decrease in pressure at 3.5 h post treatment (**Figure 3D**). This time point matches the observed NINJ1-dependent PI uptake in MEFs (**Figure S1A, Figure 3B**), kinetically linking the drop in pressure during the swelling phase with NINJ1-dependent PMR. These findings indicate that cell swelling is not caused by a sharp rise in osmotic pressure due to water influx as assumed previously, as we observed no increase in pressure. Instead, a slow expansion at constant hydrostatic pressure drives a volume increase. In WT cells, this expansion proceeds until NINJ1 lesions open, resulting in a dissipation of the hydrostatic pressure, while in the absence of NINJ1 the pressure remains constant as no plasma membrane lesions are formed.

The actin cytoskeleton is normally attached to the cell membrane and the force it exerts on the membrane participates in maintaining a constant intracellular pressure and volume[28]. However, during ferroptosis, we observed a decrease in intracellular pressure (**Figure 3B**) but an increase in cell volume (**Figure 1H&I**). To determine if changes in the actin cytoskeleton could explain these results, we fixed WT and *Ninj1* KO MEFs at 1-6 h post ML162 addition and stained for filamentous actin (F-actin) with phalloidin. We observed a striking loss in F-actin signal in both genotypes starting at 3 h post ML162 addition (**Figure 3E**). Quantifying the F-actin signal revealed a decrease in signal intensity in WT cells beginning at 2 h post ML162 addition with a precipitous decrease at 3 h in both WT and *Ninj1* KO cells (**Figure 3F**). In agreement with the data in the MEFs, we also observed a loss in F-actin signal in BMDMs at 3 h post ML162 addition (**Figure S5A**), confirming that loss of F-actin occurs in multiple cell types during ferroptosis. Since the loss of F-actin coincides with the swelling phase, we hypothesize that a loss of the actomyosin cortex during ferroptosis untethers the plasma membrane from the cytoskeleton, allowing the cell to expand without a concomitant rise in hydrostatic pressure.

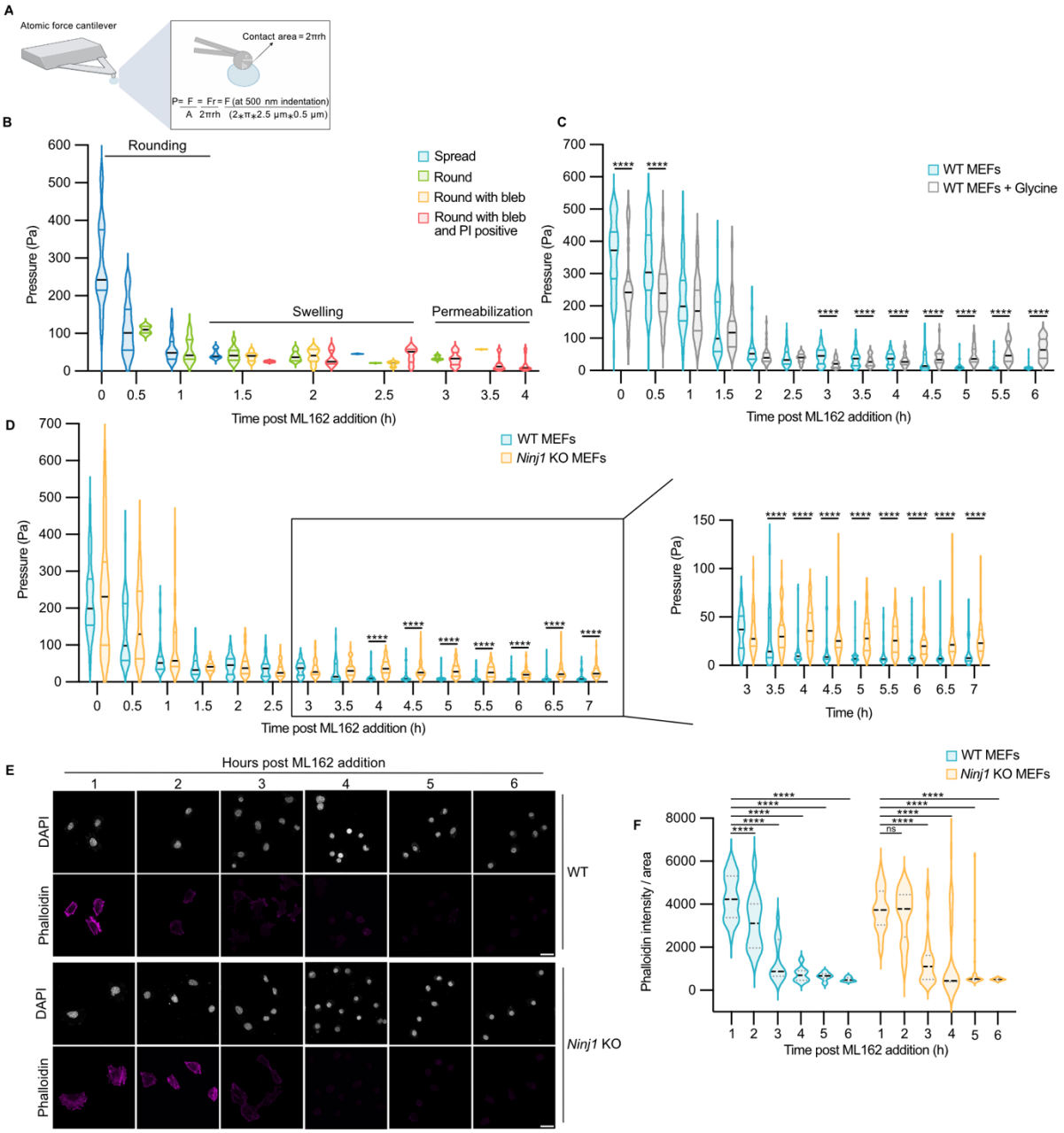

Figure 3 Cell swelling does not lead to a rise in intracellular pressure. A Schematic of an atomic force cantilever equipped with a bead to detect intracellular pressure with derivation of pressure measurement. **B-D** Violin plots of pressure measurements of MEFs treated with ML162 for the indicated times. Black bars indicate the median and gray bars are quartiles **B** Measurements performed in the presence of PI. Cells were visually separated into morphological categories. **C** Measurements performed in the presence of absence of 50 mM glycine for the indicated times. Glycine was added to cells after the 0 h measurement. **D** Pressure measurements in WT and *Ninj1* KO MEFs for the indicated times. An inset shows 3-7 h with a reduced y-axis. **E** Confocal images of DAPI and Phalloidin from WT and *Ninj1* KO MEFs at the indicated times post ML162 addition. Scale bar 30 µm. **F** Quantification of the Phalloidin signal intensity normalized to DAPI signal intensity. Data in A-D measure a total of 27-48 cells at each time point from at least 2 independent experiments. Data in E and F are representative of 3 independent experiments. Data in C and D were analyzed by multiple Mann-Whitney tests. Data in F were analyzed by 2-way ANOVA followed by Šídák's multiple comparisons tests, **** p<0.0001.

Both NINJ1 and NINJ2 oligomerize in dying cells, but only NINJ1 induces PMR

To better understand the oligomeric state of NINJ1 prior to membrane rupture, we turned to NINJ2, which shares 67% percent sequence identity with NINJ1, but is unable to permeabilize cells[9]. Intriguingly, despite its inability to permeabilize membranes, recombinant NINJ2 still forms filaments *in vitro*, which share their fence-like architecture stabilized by a kinked helix α1-α2 with NINJ1 filaments[13]. Given these findings, we first asked if NINJ2 oligomerizes in the plasma membrane during cell death. We expressed NINJ2-GFP in *NINJ1/2* dKO (double knock-out) HeLa cells and monitored the cells by live cell microscopy following ferroptosis induction in the presence of DRAQ7. We observed that NINJ2 formed filamentous oligomers on the basal plane of cells and, even though NINJ2 has previously been shown not to induce PMR[9], we eventually also observed limited DRAQ7 influx in these cells (**Figure 4A**). We then turned to total internal reflection fluorescence (TIRF) stochastic optical resolution microscopy (STORM) to further elucidate the molecular organization of NINJ2-GFP filaments in the plasma membrane. As previously observed for NINJ1[14], we found a homogeneous distribution of NINJ2-GFP in the membrane of untreated cells, which became more aggregated after induction of ferroptosis, forming filaments and clusters (**Figure 4B**). Quantifying the distribution of sizes of clusters (radius of gyration (Rg)) confirmed that the NINJ2 clusters were significantly larger than NINJ2 structures found in the untreated control cells (**Figure 4C**).

We next compared the speed of NINJ1 and NINJ2 oligomerization by performing inhomogeneity analysis, as done previously[14,30], and found that both proteins oligomerized with similar speed (**Figure 4D**), suggesting that NINJ1 and NINJ2 most likely respond to the same signal in dying cells and that their oligomerization follows a similar mechanism. However, when comparing the rate of DRAQ7 uptake induced by oligomeric NINJ1 or NINJ2, we found that while NINJ1 expression in *NINJ1/2* dKO HeLa cells resulted in a rapid DRAQ7 influx upon ferroptosis induction, NINJ2 induced DRAQ7 uptake proceeded with much slower kinetics. Indeed, the rate of DRAQ7 uptake was comparable to *NINJ1/2* dKO HeLa cells expressing a control protein, HA^{TMD}-GFP (**Figure 4E**), indicating that the observed DRAQ7 uptake (**Figure 4E**) was largely NINJ2-independent. Thus, while both NINJ1 and NINJ2 can form filamentous oligomers, NINJ2 filaments are defective in inducing plasma membrane permeabilization, further confirming that oligomerization of ninjurin family members and PMR are two distinct events that are controlled by different signals.

Given the strikingly similar architecture of NINJ1 and NINJ2 filaments, we wondered if these proteins might form heteromeric structures in dying cells, and if NINJ2 might prevent NINJ1 from inducing PMR. To test if the proteins could interact before and after cell death induction, we co-transfected HEK293T cells with NINJ1 and NINJ2 with each protein tagged with either

GFP or mCherry in both possible combinations and performed immunoprecipitation (IP) using an anti-GFP nanobody (GFP-Trap). We also performed a control IP where we expressed the GFP-tagged membrane protein HA^{TMD} in the presence of either NINJ1- or NINJ2-mCherry. Transfections were performed in HEK293T cells expressing DmrB-caspase-1[31] allowing us to induce death with the small molecule B/B homodimerizer. We immunoprecipitated both NINJ1-GFP and NINJ2-GFP in the presence and absence of B/B. At resting state, in the absence of B/B, NINJ1 co-immunoprecipitated a small amount of NINJ2 and NINJ2 co-immunoprecipitated a slightly greater amount of NINJ1, indicating an interaction between NINJ1 and NINJ2 even in the absence of cell death (**Figure 4F**). In dying cells (+B/B) there was an increased interaction between NINJ1 and NINJ2, demonstrated by an increase in the amount of NINJ2 immunoprecipitated by NINJ1, and vice versa. We observed no non-specific interaction of HA^{TMD} with either NINJ1 or NINJ2, validating the specificity of these IPs. To independently confirm this observation, we performed confocal microscopy of NINJ1-mCherry and NINJ2-GFP co-expressed in HeLa cells and observed co-localization of the proteins at both resting state and after ferroptosis induction (**Figure S6A**). Given that confocal microscopy has lower resolution to determine co-localization, we turned to two-color super resolution microscopy using a GFP nanobody and mEos. With two-color super resolution microscopy, we detected little overlap of NINJ1 and NINJ2 in untreated cells, but greater overlap in ferroptotic cells, consistent with our IP results (**Figure S6B**).

Given that these data implied the formation of hetero-oligomeric NINJ1/NINJ2 filaments, we next tested if such mixed filaments were able to permeabilize the plasma membrane by measuring DRAQ7 uptake after ferroptosis induction in cells expressing both NINJ1 and NINJ2. Interestingly, we found that ferroptotic cells expressing NINJ1 and NINJ2 displayed an intermediate speed of DRAQ7 uptake, which was slower than DRAQ7 uptake in ferroptotic cells expressing only NINJ1, but faster than in ferroptotic cells expressing only NINJ2 (**Figure 4E**).

In summary these data show that NINJ1 and NINJ2 share the ability to oligomerize during death into heteromeric filaments during cell death, but that filaments formed by NINJ2 lack the ability to efficiently induce PMR upon cell swelling.

The unstructured N-terminus of NINJ1 licenses its lytic ability

We next asked which region of the NINJ1 protein confers rapid permeabilization compared to the slower kinetics of NINJ2-mediated permeabilization of the plasma membrane. NINJ1 and NINJ2 share 76% sequence similarity in their structured region but show a more variable sequence in their N-terminus, with NINJ1 having a longer N-terminal region[27]. We reasoned

that since both proteins polymerized with similar kinetics and formed similar filaments *in vitro*, the ability to respond to cell swelling might lie within the more variable N-terminal region.

We therefore made chimeras of NINJ1 and NINJ2, beginning by replacing the N-terminal 30 amino acids (aa) of the NINJ2 N-terminus (N-term) with the 44aa of the NINJ1 N-term, (chimera 1) (**Figure 4G, Figure S6C**). By using our single-cell assay of DRAQ7 influx during ferroptosis we observed that chimera 1 permeabilized cells as quickly as NINJ1, indicating that the N-term of NINJ1 was sufficient to confer lytic activity onto NINJ2 (**Figure 4H**). To better delineate if a specific region within the N-term is responsible for faster permeabilization, we aligned the N-term of NINJ1 and NINJ2 and divided the NINJ1 N-term into 4 sub-regions: A, B, C and D (**Figure 4G**) and either swapped (A,C,D) or inserted (B) each of these 4 regions into the NINJ2 N-term. While NINJ2 containing regions A, B or C from NINJ1 did not show enhanced plasma membrane permeabilizing ability (**Figure S6D,** chimeras 2-4), swapping in NINJ1 aa35-43 (region “D”, chimera 6), which is closest to the structured part of the protein, was sufficient to confer rapid permeabilization activity on NINJ2 (**Figure 4H**). Confocal microscopy confirmed that all chimeras were localized to the plasma membrane and underwent clustering during ferroptosis (**Figure S6E**).

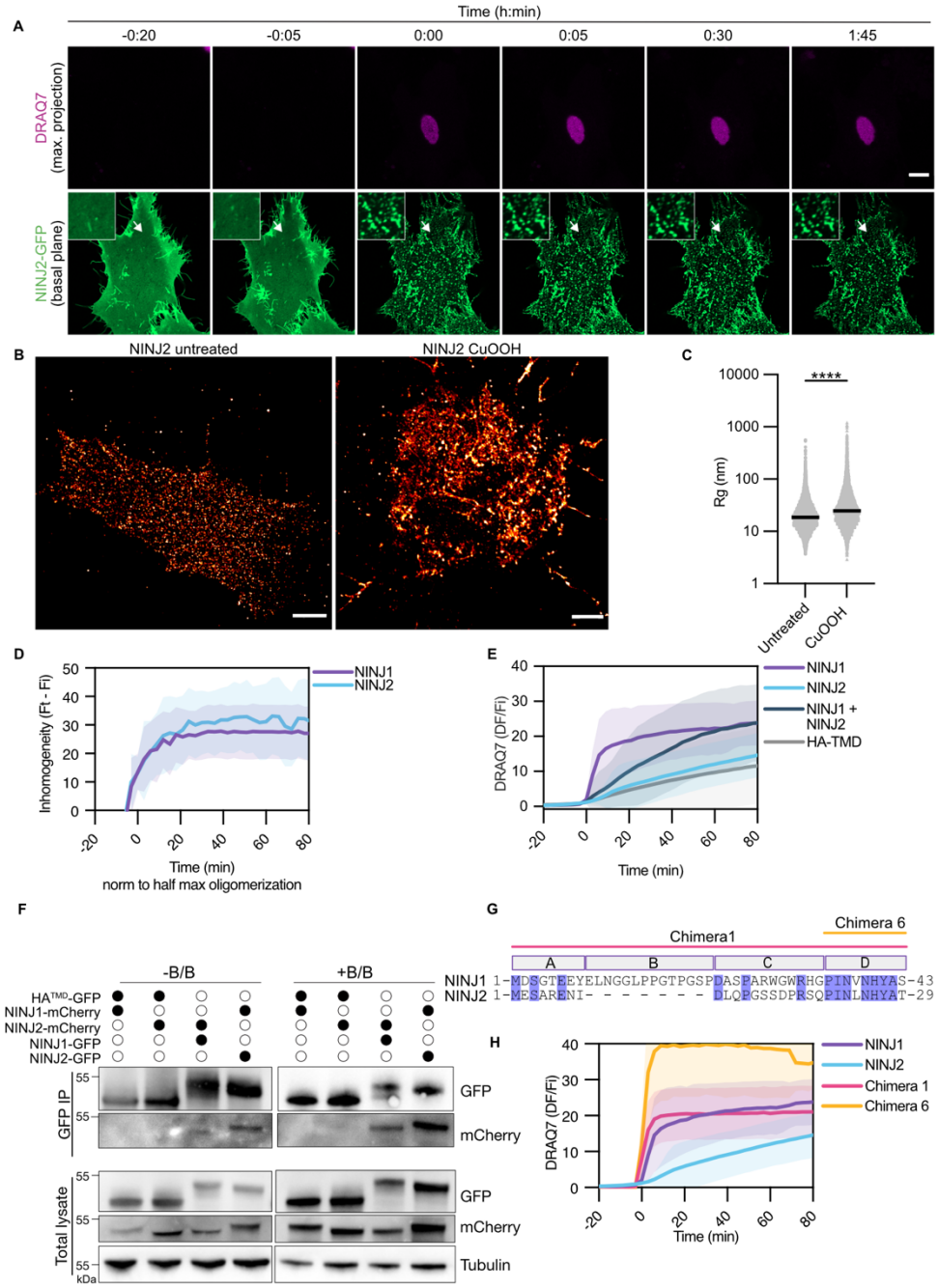

Figure 4 The N-terminus of NINJ1 endows NINJ2 with the ability to rupture the plasma membrane. A Live cell imaging of *NINJ1/2* dKO HeLa cells expressing NINJ2-GFP in the presence of CuOOH and DRAQ7. Images show the NINJ2-GFP expression at the basal plane and the influx of DRAQ7 with a maximum intensity projection from a z-stack to track plasma membrane permeabilization. Time is normalized to the onset of the increase in DRAQ7. Scale bar 10 µm. **B** STORM images of untreated or CuOOH-treated HeLa cells expressing NINJ2-GFP. Scale bar 2 µm. **C** Radius of gyration (R_g) for each identified NINJ2 cluster. Plots show the distribution of all identified clusters from two independent experiments, lines indicate median values. **D** Quantification of the distribution inhomogeneity of NINJ2-GFP in HeLa cells after treatment with CuOOH where the oligomerization of each protein is normalized to half-maximal oligomerization. **E** DRAQ7 intensity measured over time from maximum intensity projections. Live cell imaging performed on HeLa cells expressing the indicated construct and treated with CuOOH in the presence of DRAQ7. Time 0 indicates the first detectable DRAQ7 uptake. **F** Reciprocal GFP-trap IPs of GFP tagged NINJ1 or NINJ2 in the presence of HA^{TMD}-mCherry or mCherry tagged NINJ1 or NINJ2 in HEK293T cells expressing DmrB-caspase-1. The addition of B/B activates caspase-1 dimerization and induces death. Tubulin serves as a loading control. **G** Alignment of the N terminus of human NINJ1 and NINJ2 with regions used for making chimeras shown above in purple. Conserved residues between the two proteins are highlighted in

purple. **H** DRAQ7 intensity as in (**E**) for the indicated constructs. Data in A is representative of 3 independent experiments. STORM (B,C) was performed in duplicate. Data in E and H are mean ± SD from 3 independent experiments and 10-30 cells per condition. Data in F are representative of 3 independent experiments. Data in C were analyzed using Student's unpaired two-sided *t*-test, **** $p<0.0001$.

Overall, these data demonstrate that both NINJ1 and NINJ2 oligomerize with similar kinetics during ferroptosis, but that only NINJ1 filaments can create membrane lesions. Moreover, the ability to transition from inactive filaments to filaments forming membrane lesions depends on a short stretch of amino acids immediately preceding helix α1 in filamentous NINJ1.

Discussion

The mechanism by which NINJ1 ruptures the plasma membrane of dying cells has been a subject of much interest in recent years[9]. Here, based on insights from biochemical, biophysical and cell biology experiments we propose that NINJ1-induced PMR proceeds by a 2-step mechanism. We postulate that an initial trigger, signal 1, induces the dissociation of autoinhibited NINJ1 dimers thereby leading to the formation of NINJ1 filaments[12]. Initially these filaments remain inactive, possibly because two filaments associate via their hydrophilic faces to form a closed double filament zipper[14]. However, once cells swell, inactive NINJ1 filaments will activate, forming membrane lesions. This is consistent with a model in which double filament zippers open due to membrane tension and mechanical stresses. We thus propose that oligomeric NINJ1 filaments serve as 'weak links' in the membrane, acting as breaking points that will destroy membrane integrity once cells fail to control their volume, as is the case during cell death. This kind of programmed membrane destruction could alert the immune system through DAMP release and exposure of cellular components that might not otherwise be accessible. This mechanism might play an important role during apoptosis, where the formation of NINJ1 filaments might serve as a back-up strategy to induce cell lysis and inflammation, in case efferocytosis fails to remove apoptotic cells. Indeed, NINJ1 has been observed to induce secondary necrosis in tissue culture[9], but it remains to be determined how and when NINJ1 is activated after apoptosis induction.

What constitutes 'signal 1' and results in NINJ1 oligomerization remains to be determined, however it might be linked to the scrambling of plasma membrane lipid asymmetry as proposed before[14]. Indeed, a recent preprint found that Ca^{2+} influx and lipid scrambling caused by TMEM16F results in NINJ1 activation after ionomycin treatment[20]. In agreement with these findings, we also find that ionomycin treatment leads to Ca^{2+}-dependent NINJ1 oligomerization; however, we did not test if NINJ1 activation is caused due to phosphatidylserine scrambling or occurs downstream of metabolic death of the cell, which we also observed following ionomycin treatment. While we do not observe a Ca^{2+} dependency for NINJ1 activation in ferroptosis, it is possible that phospholipid scrambling in ferroptosis is Ca^{2+}-

independent or that lipid peroxidation-induced changes to the biophysical properties of the membrane bypasses the requirement for lipid scrambling.

We propose that increased cell volume constitutes 'signal 2', functionalizing NINJ1 filaments to form membrane lesions, as inhibiting cell swelling with osmoprotectants blocks PMR without affecting NINJ1 oligomerization. This is consistent with a previous report that noted that blocking cell swelling inhibits NINJ1 activation during cell death[11]. The same report suggested that cell swelling or shrinking using hypo- or hypertonic media was sufficient to activate NINJ1 and cause cell lysis around 6-8 h post treatment[11]. However, our data suggest that swelling cells with hypotonic media reduces the general viability of cells considerably, likely leading to NINJ1 oligomerization as a consequence of cell death rather than the change in cell size. These data are consistent with a two-step hypothesis where swelling alone - in the absence of the first signal to induce the formation of NINJ1 oligomers - is insufficient to drive the whole process. While our study focuses on NINJ1-mediated PMR during ferroptosis, cell swelling is known to occur during other forms of necrotic cell death including pyroptosis[24,25] and secondary necrosis[32], thus it is likely that swelling also functionalizes NINJ1 lesions in these contexts.

It has long been believed that cell swelling is caused by increased intracellular hydrostatic pressure, which could push on NINJ1 filaments thus opening a zipper or extracting a NINJ1-solubilized membrane disc[14,15,27]. However, our AFM measurements refute this theory and show that cell swelling correlates with a phase of constant internal pressure until the formation of NINJ1 lesions, which cause an additional pressure drop. Since we find that this swelling phase correlates with a loss of actin during ferroptosis, we propose that loss of cortical actin allows the plasma membrane of dying cells to expand and swell once cells lose the ability to control their osmolarity. This swelling occurs without increased hydrostatic pressure, since the cortical actin can no longer counteract the expansion of the cell. Cell swelling should nevertheless result in increased membrane tension[17,18], which could represent the mechanical force that NINJ1 was recently proposed to sense in the membrane of cells[33].

Interestingly, we find that NINJ2 shares the ability to oligomerize with NINJ1 and that it can form filaments of similar size, while being deficient in inducing PMR, consistent with previous reports[9]. It has been proposed that NINJ2 filaments have a fixed vertical curvature, which is not present in NINJ1 filaments, preventing the formation of lesions and potentially explaining why NINJ2 does not permeabilize membranes[13]. Given our findings that NINJ1 activation proceeds by a 2-step mechanism, we propose an alternative explanation in that NINJ2 forms filaments or double-filament zippers that are more stable than the respective NINJ1 structures, due to the NINJ2 N-terminus, and that these structures are able to withstand tension increases

during swelling. It remains to be defined if the region of the NINJ1 N-terminus that we find that can confer lytic capabilities does so by altering the morphology of filaments and/or the propensity of filaments to disassociate and form lesions.

In conclusion, we show that NINJ1 activation is a two-step process where oligomers are first formed and then secondly functionalized to form lesions (**Figure 5**). The formation of NINJ1 lesions depends on cell swelling, but not an increase in intracellular pressure. Similar to NINJ1 in the presence of osmoprotectants, NINJ2 can also be oligomeric in the membrane without lysing cells; however, it can be endowed with lytic properties through modifications in its unstructured N-term. It remains to be shown what goal such a 2-step mechanism would serve. As discussed, it might serve to induce cell lysis and inflammation in case apoptotic cells are not cleared, but what would be its function in other forms of cell death remains to be investigated. Another possibility is that ninjurins serve to locally increase rigidity and stabilize the plasma membrane around regions of Ca^{2+} influx and lipid scrambling, thus contributing to the repair of these regions, but that this mechanism gets overwhelmed during cell death, increasing the rigidity of the whole cell, thus making it susceptible to rupture upon swelling. It is clear that additional studies into the role of ninjurins in homeostasis and disease are needed to solve these outstanding questions.

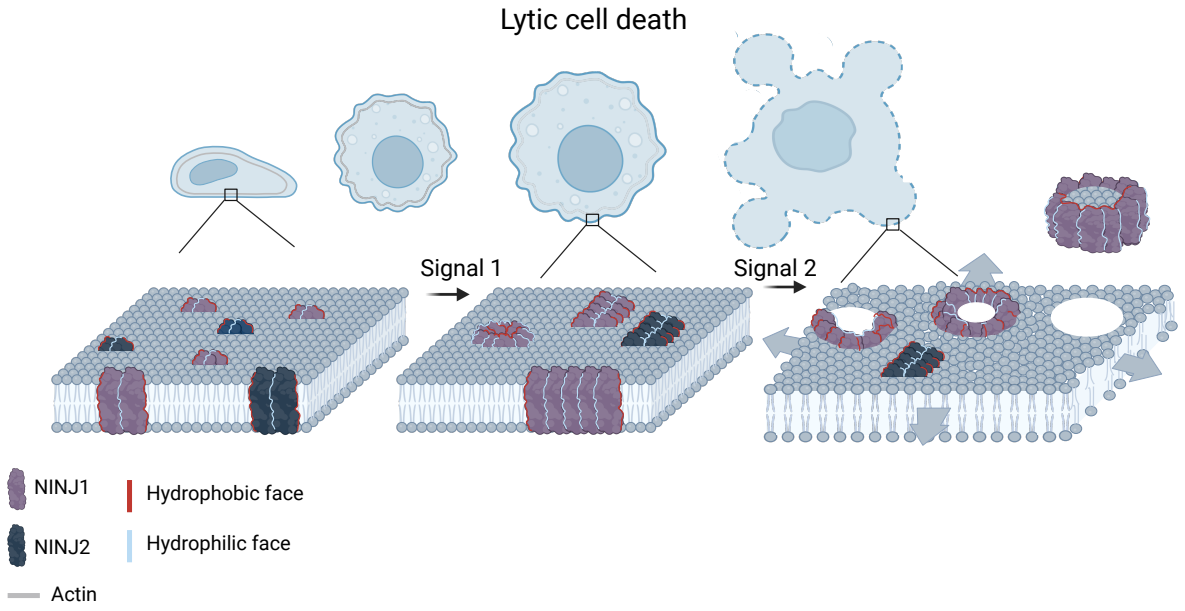

Figure 5 NINJ1-mediated PMR is a two-step process. Schematic of the proposed model of NINJ1 mediated PMR and timeline of corresponding cellular events. Upon the induction of lytic cell death, there is an initial drop in intracellular pressure and influx of Ca^{2+}. Temporally, we then observe a loss of F actin followed by NINJ1 activation characterized by reorganization of autoinhibited dimers into oligomers. Cellular volume then increases resulting in NINJ1 lesion opening and followed by a second drop in the remaining intracellular pressure. Finally, cellular DAMPs exit the cell through NINJ1 lesions. NINJ1 oligomers have a hydrophobic and a hydrophilic face. Different models of NINJ1 oligomerization suggest either that the hydrophilic face repels lipids with oligomers remaining in the membrane or that the hydrophobic face of the filament solubilizes membrane discs.

Acknowledgements

EH is supported by EMBO postdoctoral fellowship ALTF 27-2022. PB is supported by grants from the Swiss National Science Foundation (310030B_198005 and 310030_219286). DM is supported by a grant from the Swiss National Science Foundation through the NCCR Molecular Systems Engineering. VP is supported by grant ANR-22-CE15-0032-01. CS acknowledges support by the Helmholtz Association (VH-NG-1526).

We wish to thank the staff of the Cellular Imaging Facility and Animal Facility at the University of Lausanne for their crucial work maintaining microscopes and managing mouse colonies and all members of the Broz lab for helpful discussions and feedback. We thank Dr. Vishva Dixit (Genentech Inc.) for sharing the anti-NINJ1 antibody, Mathieu Bertrand (VIB, Ghent) for sharing the WT and *Ninj1* KO MEFs and Dr.Romeo Ricci (University of Strasbourg, CNRS, France) for sharing Piezo1$^{fl/fl}$Piezo2$^{fl/fl}$LysM-Cre BMDMs. We thank Aaron Ponti (Single cell facility, D-BSSE) for his image processing assistance.

Author contributions

Conceptualization: EH, EMB, PB
Investigation: EH, EMB, GA, SM, HL, LB, CS, MA, JCS, IG
Data analysis and visualization: EH, EMB, GA, SM, CS, MA, JCS
Writing - first draft: EH, EMB, PB
Writing - revisions: EH, EMB, PB, GA, SM
Supervision and funding acquisition: PB, EH, VP, DM, CS
The authors agree that EH and EMB can list their own names first when referring to this manuscript.

Competing interest statement

The authors declare no conflicts of interest.

Data and material availability

All data are available in the main and supplemental figures. All plasmids will be made available on Addgene. Any requests for materials should be made to PB.

Materials and methods

Cell culture

BMDMs were differentiated from bone marrow isolated from C57BL/6J WT and *Ninj1*$^{-/-}$ mice as previously reported using L929 cell supernatant as a source of M-CSF. Piezo1$^{fl/fl}$Piezo2$^{fl/fl}$LysM-Cre BMDMs and the LysM-Cre controls were obtained from Romeo Ricci[23]. BMDMs were maintained in DMEM high glucose (Thermo Fisher Scientific) supplemented with 10% FCS (BioConcept), 20% MCSF, 1% NEAA (Thermo Fisher Scientific), 10 mM HEPES (Thermo Fisher Scientific), and 1% Pen/Strep (BioConcept) and stimulated on days 9 to 10 of differentiation. WT and *Ninj1*$^{-/-}$ iBMDMs were previously reported[10] and maintained in DMEM supplemented with 10% FCS, 10% MCSF, 1% NEAA and 10 mM HEPES. WT and *Ninj1* KO MEFs were obtained from Mathieu Bertrand[11] and maintained in DMEM supplemented with 10% FCS, 2 mM L-Glutamine (Sigma Aldrich), and 400 µM sodium pyruvate (Thermo Fisher Scientific). HeLa cells were maintained in DMEM supplemented with 10% FCS. 293T-DmrB-caspase1 cells were previously described[31] and were maintained in DMEM supplemented with 10% FCS. All cells were maintained at 37ºC, 5% CO_2 in humidified incubators. All cell lines are regularly tested in the lab for mycoplasma contamination and are mycoplasma free.

Animals

All experiments involving animals were performed under the guidelines of and with approval from the cantonal veterinary office of the canton of Vaud (Switzerland), license number VD3257. All mice were bred and housed at a specific-pathogen-free facility at 22 ± 1 C° room temperature, 55 ± 10% humidity and a day/night cycle of 12h/12h at the University of Lausanne. *Ninj1*$^{-/-}$, *Caspase1/11*$^{-/-}$ and *Ripk3*$^{-/-}$ mice were described previously[14,34,35].

Plasmids

All cloning for plasmids in this manuscript was done with Infusion cloning (Takara), following the manufacturer's instructions. All plasmids from this manuscript will be available on Addgene. NINJ1-GFP (Addgene 208779) is previously published[10,14]. Plasmids used in this study: pMT HA^{TMD}-mCherry, pMT HA^{TMD}-GFP, pLVX NINJ2-GFP, pLVX NINJ1-mCherry, pLVX NINJ2-mCherry, pLVX Chimera 1 - GFP, pLVX Chimera 2 - GFP, pLVX Chimera 3 - GFP, pLVX Chimera 4 - GFP, pLVX Chimera 5 - GFP, pLVX Chimera 6 - GFP, pLVX NINJ1-mEOS.

CRISPR editing

NINJ1/2 DKO HeLa cells were made by lentiviral transduction of HeLa cells with Cas9 and a sgRNA to *NINJ1* (sequence: GAGGAGTACGAGCTCAACGG) on a blasticidin resistance

cassette (pLentiCRISPR Blast, gift of A. Jourdain, University of Lausanne) and then secondarily transducing with lentivirus harboring a *NINJ2* (sequence: CATGGCGTTGGACATGAACA) targeting sgRNA and a zeocin resistance cassette. Lentivirus was made by seeding 1.5 x 10^6 HEK 293T cells the day before in a 6 well dish. The following day 250 ng VSVG, 1250 ng psPAX2 and 1250 ng of the sgRNA-containing vector were transfected with 8.25 µL of LT-1 (Mirus). Media was changed the next morning to 4 mL DMEM supplemented with 10% FBS and 1% BSA (Sigma Aldrich). Lentivirus containing supernatants were harvested 48 h post transfection and filtered through a 0.22 µm syringe filter. Recipient cells were spinfected at 500 x *g* for 90 min with 1 mL (Cas9 containing) or 200 µL (sgRNA only containing vector) of virus containing supernatant in the presence of 8 µg/mL polybrene (Sigma Aldrich). HeLa cells were selected with 5 µg/mL blasticidin (Invivogen) and 200 µg/mL zeocin (Invivogen).

Cell stimulations

All cells were seeded the day before stimulation and, unless indicated, stimulations were performed in OptiMEM (Thermo Fisher Scientific). Unless specifically indicated, ferroptosis was induced as follows: 750 µM cumene (Sigma Aldrich) for BMDMs and HeLa or ML162 (Sigma Aldrich) at 5 µM for BMDMs or 10 µM for MEFs or RSL3 (Lubioscience) at 5 µM for BMDMs. Ionomycin (Abcam) was used at 4 µM. Pyroptosis was induced with 5 µM nigericin (Sigma Aldrich) for 4 h. Apoptosis was triggered with 100 ng/mL TNFα (Peprotech) + 500 nM AZD5582 (Lubioscience) for 6 h. Necroptosis was induced with 100 ng/mL TNFα + 500 nM AZD5582 + 20 µM zVAD (Invivogen) for 6 h.

OptiMEM was supplemented with sucrose (Sigma Aldrich), PEG600 (Fuka) or PEG6000 (Santa Cruz) as indicated. Hypotonic media was made by mixing microbiology grade H_2O (BioConcept) with OptiMEM. 76 mOsm solution was obtained by mixing 80% H2O with 20% OptiMEM. Before incubation, media was removed from cells, they were washed once with 76 mOsm solution before proceeding with the experiment. Osmolarity of all solutions was measured on a vapor pressure osmometer (Wescor).

To compare cell death in the presence and absence of calcium cells were stimulated in DMEM or calcium free DMEM (Thermo Fisher Scientific) + 10 µM BAPTA-AM (Tocris).

Calcium measurements

BMDMs were loaded with Fluo8 (Abcam) according to the manufacturer's instructions at the same time as ML162 treatment. Following stimulation cells were imaged on an Incucyte using a 10X objective with images every 10 min.

Images were analyzed using Incucyte software by measuring the integrated density of the GFP signal from the images. At least 3 images were captured per well with 3 technical replicates per experiment.

Western blotting

For crosslinking experiments stimulations were either performed directly in PBS containing Ca^{2+} and Mg^{2+} (Thermo Fisher Scientific) or, after stimulation media was changed to PBS with Ca^{2+} and Mg^{2+} to perform crosslinking. At the endpoint 25 mM bis(sulfosuccinimidyl)suberate (BS^3, Thermo Fisher Scientific) dissolved in water was spiked into the well to a final concentration of 3 mM and cells were incubated at room temperature for 5 min. The reaction was quenched through the addition of an equal volume of 40 mM Tris-HCl pH7.4 and incubated for 15 min at room temperature. Supernatant was then aspirated and cells lysed in sample buffer (NuPage LDS sample buffer (Thermo Fisher Scientific) + 66 mM Tris-HCl pH7.4, 2% SDS (PanReac) + 10 mM DTT (Thermo Fisher Scientific). Samples were boiled at 97°C for 7 minutes.

Proteins were precipitated from the supernatant by chloroform/methanol extraction. Supernatants were mixed with 1 volume of methanol (Thermo Fisher Scientific) and 0.3 volumes chloroform (Sigma Aldrich), vortexed then centrifuged at 14,000 x *g* for 10 min at 4°C. The upper phase was discarded and 1.3 volumes MeOH added before repeating the vortex and centrifugation steps. The supernatant was discarded and the pellet air dried before resuspending in the corresponding cell lysate.

Samples were then separated on 4-12% BisTris SDS-PAGE gels (Merck) and transferred to nitrocellulose membranes (Amersham GE) using a Transblot Turb (Bio-Rad). Membranes were blocked in 5% skimmed milk, all antibodies were diluted in 5% milk and incubated either overnight at 4°C or for 1 h at room temperature.

Antibodies used: NINJ1 (Genentech Inc, clone 25, 1:8000), H3 (Cell Signaling Technologies 3638S 1:2000), Tubulin-HRP (Abcam ab40742, 1:5000), GFP (Enzo Life Sciences ALX-210-199-R100, 1:1000), mCherry (Abcam, ab125096, 1:1000), Caspase-1 (Adipogen AG-20B-0042-C100, 1:1000), Caspase-3 (Cell Signaling Technology 9662S, 1:1000), GSDMD (Abcam ab209845, 1:1000), MLKL (EMD Millipore MABC604, 1:1000), MLKL pS345 (Abcam ab196436, 1:1000), anti-rabbit IgG HRP (SouthernBiotech 4030-05, 1:5000), anti-mouse IgG HRP (SouthernBiotech 1034-05, 1:5000).

Live cell imaging

Live cell imaging was performed on a Zeiss LSM800 equipped with heating and CO_2 control using a 63X 1.4 NA oil immersion objective with autofocus (Zeiss Definite Focus.2 system) and data were acquired using Zeiss ZEN 2 software.

BMDMs were seeded at 75,000 cells per well of iBidi 8 well slides the day before stimulation. Cells were stained with CellBrite Orange (Biotium, 1:200 in OptiMEM) for 20 minutes, washed three times in warm OptiMEM and then stimulated as indicated before immediately placing them on the microscope. DRAQ7 (Biolegend) was present at 300 nM. Cells were imaged every 3 min with 10-12 Z planes per image. At least 6 fields of view were imaged per experiment and 3 independent experiments performed.

HeLa cells were seeded at 10,000 cells per well in the afternoon, transfected the following morning using XtremeGene9 (Sigma Aldrich), then NINJ1 expression was induced with 2 ug/mL doxycycline (Sigma Aldrich) in the afternoon before imaging the following day in OptiMEM in the presence of 300 nM DRAQ7 and 750 µM CuOOH. Cells were imaged every 3 min with 4-6 Z planes per image. 17-29 cells from 2-3 biological replicates were quantified in each condition.

Fixed cell imaging

HeLa cells were seeded on glass coverslips in 12 well dishes at 25,000 cells per well in the morning. Transfections were performed the same afternoon using XtremeGene9. The following morning cells were treated as indicated in figure legends. Samples were fixed in 4% PFA (Electron Microscopy Sciences) for 10 min, washed with PBS, permeabilized with 0.05% saponin and blocked with 1% BSA in PBS. For Airyscan imaging samples were treated with Hoechst 33342 (ThermoFisher Scientific, 1:1000).

To image actin in MEFs, WT and *Ninj1* KO MEFs were seeded in 8 well glass bottom dishes (IBIDI, cells in focus) and left to adhere overnight. To induce ferroptosis, cells were treated with 10 µM ML162 and fixed in 4% (v/v) paraformaldehyde (PFA) at different timepoints. To permeabilize the cell membrane and prevent unspecific binding, cells were incubated for one hour at room temperature in a 5% (w/v) serum albumin (Sigma) in 0.2% (v/v) Triton-X in PBS (Gibco). Fixed cells were stained for nucleus (DAPI, Invitrogen) and F-actin (Alexa Fluor 647, Life Technologies) and images collected with a Leica SP8 falcon confocal microscope.

To image actin in BMDMs cells were seeded on glass coverslips at 150,000 cells we per well, treated as indicated then fixed in 4% PFA for 10 min. Cells were stained with Hoechst 33342

(1:5000) and Phalloidin-iFluor 647 (Abcam ab176759, 1:1000). After washing, coverslips were mounted using Vectashield PLUS and imaged on a Zeiss LSM800 laser scanning confocal microscope.

For STORM and STORM/PALM imaging, HeLa cells were seeded on 25 mm glass slides. After blocking, cells were incubated with AlexaFluor 647-conjugated anti-GFP nanobodies (FluoTax-X4, NanoTag; 1:500 dilution) in blocking buffer for 2 h. The sample was finally washed three times for 10 min in PBS. For dual color STORM/PALM, HeLa cells were transfected with NINJ2-GFP and NINJ1-mEOS.

Image analysis

All microscopy datasets were analyzed and processed with Fiji software.

The pattern of fluorescent protein-tagged constructs over time on the plasma membrane was evaluated using QuASIMoDOH[30] (Quantitative Analysis of the Spatial-distributions in Images using Mosaic segmentation and Dual parameter Optimization in Histograms) using the basal plane of cells. The distribution inhomogeneity at each time point (dt) was normalized to the distribution inhomogeneity at the initial time point of the experiment (ti). Time 0 was defined as described below.

To determine the DRAQ7 ratio a maximum projection of all imaged slices was made. An ROI was manually drawn around the nucleus and the mean pixel intensity determined within this ROI at all timepoints. The ratio was then determined using the formula $(Mean\ t - Mean\ ti)/Mean\ ti$ where ti is the value in the first frame imaged. Time 0 in all analyses is set as the first frame where this ratio exceeds 1.

To measure the diameter of cells, a straight line was manually drawn across the CellBrite image from one Z plane and the length of this line measured. The diameter was then normalized to the diameter of the cell in the first frame imaged using the formula $(Diameter\ t - Diameter\ ti)/Diameter\ ti$. For each condition a minimum of 20 cells from 3 biological replicates were analyzed.

To measure actin signal intensity in the MEFs, quantification was performed using a custom Python script (see supplementary material). Maximum projection images of actin staining were processed using Otsu thresholding to separate background from foreground and generate a binary mask. The mean fluorescence intensity and projected area were then calculated from the masked regions.

Single-molecule localization microscopy and analysis

A Nikon Ti Eclipse NSTORM microscope equipped with a 642 nm laser (F-04306-113, MPB Communications Inc.) was used for STORM imaging to switch molecules to the off state. A 405 nm laser (Cube, Coherent) was used to control the return rate of the fluorophores to the emitting state. A F73-888 quad-band dichroic (Chroma) was used to reflect the laser light on the sample. Emitted light from the sample was collected by the objective lens (Apo TIRF 100x, NA 1.49 Oil, Nikon), passed through the dichroic mirror onto an EMCCD camera (iXon DU-897D, Andor). For additional PALM imaging (Dual-color PALM STORM), we used a 405 nm (Coherent) activation laser to control the photoswitching rate of expressed molecules and a 561 nm (Sapphire, Coherent) laser to excite the photoconverted fraction. Emitted light was directed onto the camera using a dichroic mirror and filtered through a Bright Line HC 609/64 emission filter. The width of a square camera pixel corresponds to 160 nm on the sample. Imaging was performed using an established photo-switching buffer made of 50 mM Tris with 10 mM NaCl, supplemented with 10 % glucose, 50 mM MEA, 0.5 mg/mL glucose oxidase and 40 µg/mL catalase. All chemicals were purchased from Sigma. Typically, 10,000 frames were recorded per field of view with continuous laser exposure at 30 ms integration time. The microscope was controlled using NIS elements (Nikon), single-molecule localization analysis was performed using Decode[36]. Localizations were processed using custom MatLab (Mathworks) code, images were rendered using Thunderstorm[37]. Localizations were clustered using DBSCAN[38].

Cytotoxicity assays

LDH release was measured from the supernatant of cell cultures following the manufacturer's instructions (Sigma Aldrich 11644793001). 100% lysis was performed using a final concentration of 0.1% TritonX-100. Each experiment was performed in technical triplicate and for 100% and untreated conditions the average of the technical replicates obtained. The %LDH release was calculated using the formula $(Value\ sample - Value\ untreated)/(Value\ 100\% - Value\ untreated) * 100$.

Propidium iodide (PI) uptake was measured using a Cytation5 (Biotek) plate reader or Incucyte SX1 (Sartorius). Briefly, cells were stimulated in the presence of 12.5 µg/mL PI (ThermoFisher Scientific) and directly placed on the instrument for analysis. For plate reader analysis the total fluorescence intensity was measured using an excitation wavelength of 535 nm and an emission wavelength of 617 nm. For Incucyte analysis images of PI and brightfield were captured using a 10X objective with 3 images per well and the integrated density of PI signal per image calculated using Incucyte software. Data was then normalized to 100% and untreated controls. The percentage of PI uptake was then calculated using $(Value\ sample -$

$Value\ untreated)/(Value\ 100\% - Value\ untreated) * 100$. Each experiment was performed in technical triplicate.

Cellular ATP content was assayed using CellTiter-Glo 2.0 (Promega G9241) according to the manufacturer's instructions. Luminescence was read using a Spectramax ID5 (Molecular Devices) plate reader. The % cell viability was calculated using the formula $(Value\ sample/Value\ untreated) * 100$

Pressure measurements by atomic force microscopy

For pressure measurements, we employed an atomic force microscope (CellHesion, JPK Instruments, Berlin, Germany) mounted on an inverted microscope (Observer.Z, Zeiss). To maintain culture conditions (37°C and 5% CO_2) the experimental setup was placed in a temperature-controlled chamber (The Cube, Life Imaging Services) and the dish was continuously perfused with a humidified gas mixture based on synthetic air containing 5% CO_2[39]. To indent the cells, we employed triangular cantilevers (NPO, Bruker) with a 5 µm diameter colloidal bead (Kisker Biotech Gmbh & co.) glued to their free ends. The cantilevers had a nominal spring constant of 0.06 N m^{-1}. Before each experiment, the spring constant of the cantilever was measured using the thermal noise method[40]. During the experiment the cells were maintained in culture medium DMEM (31966047, Thermo Fisher Scientific) supplemented with 10% (v/v) fetal bovine serum (FBS, F9665, Sigma Aldrich), 2 mM L-Glutamine (Fisher Scientific), and 400 µM Sodium Pyruvate (Gibco)).

Single cells were indented on top of the nucleus at a constant speed of 10 µm s^{-1} until reaching a determined force setpoint. Given the major changes in pressures observed over the time course of the experiment, force setpoints were chosen between 0.5 and 6 nN, to always indent the cells by ~ 600 nm.

Pressure was calculated by dividing the force (*F*), which the beaded cantilever applied to a single cell at a defined indentation depth of 500 nm, by the area (*A*) of contact between the bead and the cell: $P = F/A$. *A* was calculated as $A = 2\pi Rh$ with *R* being the radius of the bead (2.5 µm) and *h* being the indentation depth of 500 nm. *F* was extracted from force-distance curves recording a 500 nm indentation of the bead on the cell. Force-distance curves were corrected for the cantilever deflection.

Volume measurement by fluorescence exclusion microscopy

Volume measurements were performed in PDMS culture chambers of controlled height (h = 22 µm) in OptiMEM medium supplemented with dyes conjugated with dextran molecules of

defined sizes (Alexa647-10kDa dextran from ThermoFisher Scientific and FITC-500kDa from Sigma Aldrich). Acquisitions were performed under a Leica DMi8 microscope at 37°C with a 10x magnification objective (N.A. 0.3).

PDMS molds were made with classical photolithography, a mixture of PMDS and its crosslinker (1:10, Sylgard 184 from Dow Corning) was poured onto the mold, degazed and left for reticulation at 65°C for at least 2 hours. Chambers were bonded with air plasma (Harrick Plasma). Cells were injected directly after bonding and incubated overnight at 37°C under 5% CO_2 atmosphere in high glucose DMEM supplemented with 10% (v/v) fetal bovine serum and 1% penicillin-streptomycin.

Image analysis was performed using MatLab (The MathWorks Inc.) with homemade scripts as described in Nadjar et al. 2024[25]. Briefly, cell segmentation was performed on the largest dye (FITC-500kDa dextran) and propagated to images obtained with smaller dyes. Calibration of the relation between the fluorescence intensity and pixel height was made for each field of view and each time frame[41]. Points of interest were defined by users on the basis of volume trajectories in order to extract volume and time values corresponding to swelling onset and dye entries.

PDMS is a hydrophobic material, in addition the surface-to-volume ratio in the FXm chambers is very large. This implies that hydrophobic molecules such as drugs are highly depleted by the surface of FXm chambers. To solve this issue, chambers with constant passive renewal of medium were used. Second, a large range of CuOOH concentrations was tested, no reaction was observed in the chambers below 20 mM while 1 mM was sufficient to induce ferroptosis outside the chambers.

Immunoprecipitation: GFP-Trap

$3x10^5$ HEK293T cells were seeded the day before in a 6-well plate in duplicate and transfected the following day using XtremeGene9 following the manufacturer's protocol. 24 h later cells were washed in cold PBS and then pipetted into 1.5 mL of cold PBS. Cells were pelleted at 300 x *g* for 5 min at 4°C and then lysed in 500 mL PBS + 0.1% TritonX-100 + 1 mM $MgCl_2$ + protease inhibitors (Sigma Aldrich) for 1 h on ice. Nuclei were pelleted by spinning at 20,000 x *g* for 15 min at 4°C and then supernatant (cytoplasm) was removed. 25 µl GFP-Trap magnetic agarose beads (ChromoTek) per sample were washed 3x with PBS and then added to the cytoplasmic lysate for 3 h at 4°C rotating. Beads were then separated and washed 3x with the lysis buffer on a magnet, then resuspended in 2X NuPage LDS sample buffer (Thermo Fisher Scientific) and boiled for 5 min at 95°C followed by Western blotting.

Statistical analysis

All graphs were made and statistical analyses performed using Graphpad Prism v10. Details of all analyses, including number of replicates and tests performed can be found in the figure legends. In all cases, a p value of less than 0.05 was used to determine statistical significance.

References

1. Ma, M., Jiang, W. & Zhou, R. DAMPs and DAMP-sensing receptors in inflammation and diseases. *Immunity* **57**, 752–771 (2024).
2. Silva, M. T., Do Vale, A. & Dos Santos, N. M. N. Secondary necrosis in multicellular animals: An outcome of apoptosis with pathogenic implications. *Apoptosis* vol. 13 463–482 Preprint at https://doi.org/10.1007/s10495-008-0187-8 (2008).
3. Sachet, M., Liang, Y. Y. & Oehler, R. The immune response to secondary necrotic cells. *Apoptosis* **22**, 1189–1204 (2017).
4. Vandenabeele, P., Bultynck, G. & Savvides, S. N. Pore-forming proteins as drivers of membrane permeabilization in cell death pathways. *Nat Rev Mol Cell Biol* **24**, 312–333 (2023).
5. Xia, B. *et al.* MLKL forms cation channels. *Cell Res* **26**, 517–528 (2016).
6. Xia, S. *et al.* Gasdermin D pore structure reveals preferential release of mature interleukin-1. *Nature* **593**, 607–611 (2021).
7. Pruenster, M. *et al.* E-selectin-mediated rapid NLRP3 inflammasome activation regulates S100A8/S100A9 release from neutrophils via transient gasdermin D pore formation. *Nat Immunol* **24**, 2021–2031 (2023).
8. Mehrotra, P. *et al.* Oxylipins and metabolites from pyroptotic cells act as promoters of tissue repair. *Nature* **631**, 207–215 (2024).
9. Kayagaki, N. *et al.* NINJ1 mediates plasma membrane rupture during lytic cell death. *Nature* **591**, 131–136 (2021).
10. Ramos, S., Hartenian, E., Santos, J. C., Walch, P. & Broz, P. NINJ1 induces plasma membrane rupture and release of damage-associated molecular pattern molecules during ferroptosis. *EMBO Journal* **43**, 1164–1186 (2024).
11. Dondelinger, Y. *et al.* NINJ1 is activated by cell swelling to regulate plasma membrane permeabilization during regulated necrosis. *Cell Death Dis* **14**, (2023).
12. Pourmal, S. *et al.* Autoinhibition of dimeric NINJ1 prevents plasma membrane rupture. *Nature* (2024) doi:10.1038/s41586-024-08273-4.
13. Sahoo, B., Mou, Z., Liu, W., Dubyak, G. & Dai, X. How NINJ1 mediates plasma membrane rupture and why NINJ2 cannot. *bioRxiv* (2023) doi:10.1101/2023.05.31.543175.
14. Degen, M. *et al.* Structural basis of NINJ1-mediated plasma membrane rupture in cell death. *Nature* **618**, 1065–1071 (2023).
15. David, L. *et al.* NINJ1 mediates plasma membrane rupture by cutting and releasing membrane disks. *Cell* **187**, 2224-2235.e16 (2024).
16. Devant, P. & Kagan, J. C. Molecular mechanisms of gasdermin D pore-forming activity. *Nature Immunology* vol. 24 1064–1075 Preprint at https://doi.org/10.1038/s41590-023-01526-w (2023).
17. Roffay, C. *et al.* Passive coupling of membrane tension and cell volume during active response of cells to osmosis. *Proceedings of the National Academy of Sciences* **118**, (2021).

18. Dai, J., Sheetz, M. P., Wan, X. & Morris, C. E. *Membrane Tension in Swelling and Shrinking Molluscan Neurons*. (1998).
19. Pedrera, L. *et al.* Ferroptotic pores induce Ca2+ fluxes and ESCRT-III activation to modulate cell death kinetics. *Cell Death Differ* **28**, 1644–1657 (2021).
20. Borges, J. P. *et al.* NINJ1 is activated by calcium-driven plasma membrane lipid scrambling during lytic cell death. *bioRxiv* (2024) doi:10.1101/2024.10.23.619800.
21. Syeda, R. *et al.* Chemical activation of the mechanotransduction channel Piezo1. *Elife* **4**, (2015).
22. Hirata, Y. *et al.* Lipid peroxidation increases membrane tension, Piezo1 gating, and cation permeability to execute ferroptosis. *Current Biology* **33**, 1282-1294.e5 (2023).
23. Ran, L. *et al.* KCNN4 links PIEZO-dependent mechanotransduction to NLRP3 inflammasome activation. *Sci Immunol* **8**, 4699 (2023).
24. de Vasconcelos, N. M., Van Opdenbosch, N., Van Gorp, H., Parthoens, E. & Lamkanfi, M. Single-cell analysis of pyroptosis dynamics reveals conserved GSDMD-mediated subcellular events that precede plasma membrane rupture. *Cell Death Differ* **26**, 146–161 (2019).
25. Nadjar, J. *et al.* Optogenetically controlled inflammasome activation demonstrates two phases of cell swelling during pyroptosis. *Sci Signal* **17**, (2024).
26. Borges, J. P. *et al.* Glycine inhibits NINJ1 membrane clustering to suppress plasma membrane rupture in cell death. *Elife* **11**, (2022).
27. Ramos, S., Hartenian, E. & Broz, P. Programmed cell death: NINJ1 and mechanisms of plasma membrane rupture. *Trends Biochem Sci* **49**, 717–728 (2024).
28. Stewart, M. P. *et al.* Hydrostatic pressure and the actomyosin cortex drive mitotic cell rounding. *Nature* **469**, 226–231 (2011).
29. den Hartigh, A. B., Loomis, W. P., Anderson, M. J., Frølund, B. & Fink, S. L. Muscimol inhibits plasma membrane rupture and ninjurin-1 oligomerization during pyroptosis. *Commun Biol* **6**, (2023).
30. Paparelli, L. *et al.* Inhomogeneity Based Characterization of Distribution Patterns on the Plasma Membrane. *PLoS Comput Biol* **12**, (2016).
31. Rühl, S. *et al.* ESCRT-dependent membrane repair negatively regulates pyroptosis downstream of GSDMD activation. *Science (1979)* **362**, 956–960 (2018).
32. Rogers, C. *et al.* Cleavage of DFNA5 by caspase-3 during apoptosis mediates progression to secondary necrotic/pyroptotic cell death. *Nat Commun* **8**, (2017).
33. Xu, J. *et al.* NINJ1 regulates plasma membrane fragility under mechanical tension. *Res Sq* (2024) doi:10.21203/rs.3.rs-5237916/v1.
34. Kayagaki, N. *et al.* Non-canonical inflammasome activation targets caspase-11. *Nature* **479**, 117–121 (2011).
35. Newton, K., Sun, X. & Dixit, V. M. Kinase RIP3 Is Dispensable for Normal NF-κBs, Signaling by the B-Cell and T-Cell Receptors, Tumor Necrosis Factor Receptor 1, and Toll-Like Receptors 2 and 4. *Mol Cell Biol* **24**, 1464–1469 (2004).
36. Speiser, A. *et al.* Deep learning enables fast and dense single-molecule localization with high accuracy. *Nat Methods* **18**, 1082–1090 (2021).
37. Ovesný, M., Křížek, P., Borkovec, J., Švindrych, Z. & Hagen, G. M. ThunderSTORM: A comprehensive ImageJ plug-in for PALM and STORM data analysis and super-resolution imaging. *Bioinformatics* **30**, 2389–2390 (2014).
38. Ester, M., Kriegel, H.-P., Sander, J. & Xu, X. A Density-Based Algorithm for Discovering Clusters in Large Spatial Databases with Noise. in *Second International Conference on Knowledge Discovery and Data Mining* 226–231 (AAAI, 1996).

39. Alsteens, D. *et al.* Nanomechanical mapping of first binding steps of a virus to animal cells. *Nat Nanotechnol* **12**, 177–183 (2017).
40. Hutter, J. L. & Bechhoefer, J. Calibration of atomic-force microscope tips. *Review of Scientific Instruments* **64**, 1868–1873 (1993).
41. Zlotek-Zlotkiewicz, E., Monnier, S., Cappello, G., Le Berre, M. & Piel, M. Optical volume and mass measurements show that mammalian cells swell during mitosis. *Journal of Cell Biology* **211**, 765–774 (2015).

Supplemental figures

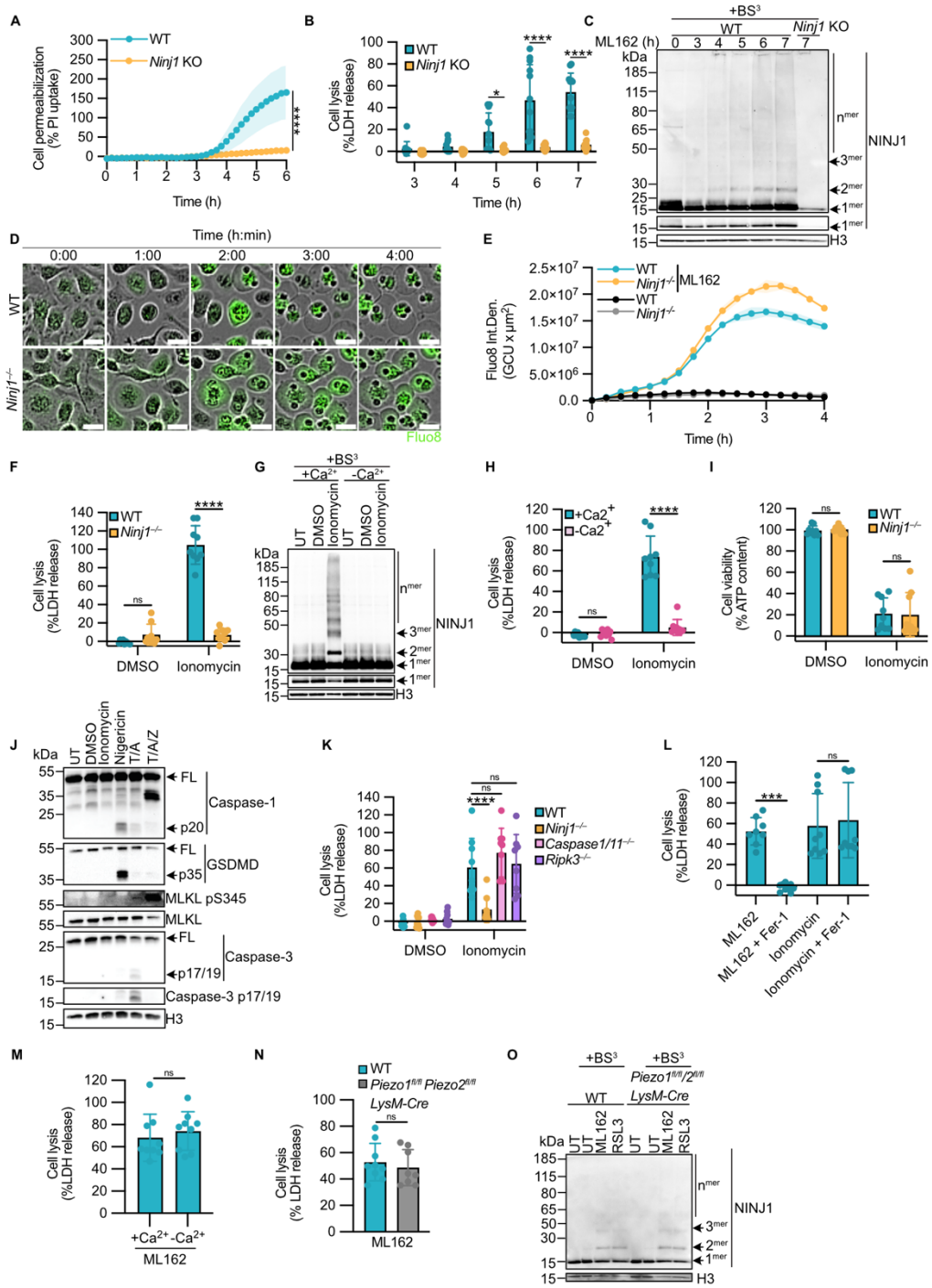

Figure S1 NINJ1-mediated plasma membrane rupture is independent of Ca^{2+}. A-C WT and *Ninj1* KO MEFs were stimulated with ML162 and analyzed for PI uptake (**A**), LDH release (**B**) and NINJ1 oligomerization by crosslinking Western blot (**C**). **D-E** WT and *Ninj1*$^{-/-}$ BMDMs were loaded with Fluo8 and stimulated with ML162 then imaged live on an Incucyte. Stills of phase contrast and GFP images are shown (**D**) along with quantification of Fluo8 signal (**E**). **F** WT and *Ninj1*$^{-/-}$ BMDMs were stimulated with DMSO or ionomycin for 2 h and supernatants analyzed for LDH release. **G&H** WT BMDMs were stimulated as indicated in DMEM with or without Ca^{2+} for 2 h and subsequently cells crosslinked and analyzed by immunoblot (**G**) and supernatants were analyzed for LDH release (**H**). **I** WT BMDMs were stimulated as indicated for 2 h and cellular ATP content measured. **J** Immunoblot of pooled proteins from supernatant and cell lysate from Pam3CSK4 primed WT BMDMs stimulated as indicated. UT: Untreated, T/A: TNFα+AZD5582, T/A/Z: TNFα+AZD5582+zVAD. **K** BMDMs of the indicated genotypes were stimulated for 2 h and LDH release into the supernatant analyzed. **L** WT BMDMs were stimulated with ML162 for 4 h or ionomycin in the presence or absence for ferrostatin-1 (Fer-1) for 2 h and LDH release into the supernatant

analyzed. **M** WT BMDMs were treated with ML162 in DMEM with or without Ca^{2+} for 4 h and LDH release analyzed. **N** WT and Piezo1$^{fl/fl}$Piezo2$^{fl/fl}$LysM-Cre BMDMs were treated with ML162 for 4 h and supernatants were analyzed for LDH release. **O** WT and Piezo1$^{fl/fl}$Piezo2$^{fl/fl}$LysM-Cre BMDMs were treated with ML162 or RSL3 for 4 h and subject to crosslinking and immunoblot with the indicated antibodies. Data in A, B, F, H, I, K, L, M and N are mean ± SD from 3 independent experiments. The blots in C, G, J and O and images in D are representative of 2-3 independent experiments. Data in E are mean ± SD from 3 technical replicates and representative of 3 independent experiments. Data in A, B, F, H, I, K and L were analyzed by 2-way ANOVA followed by Šídák's multiple comparisons tests. Data in M and N were analyzed by two-tailed Mann-Whitney test. ns not significant, * $p<0.05$, *** $p<0.001$, **** $p<0.0001$.

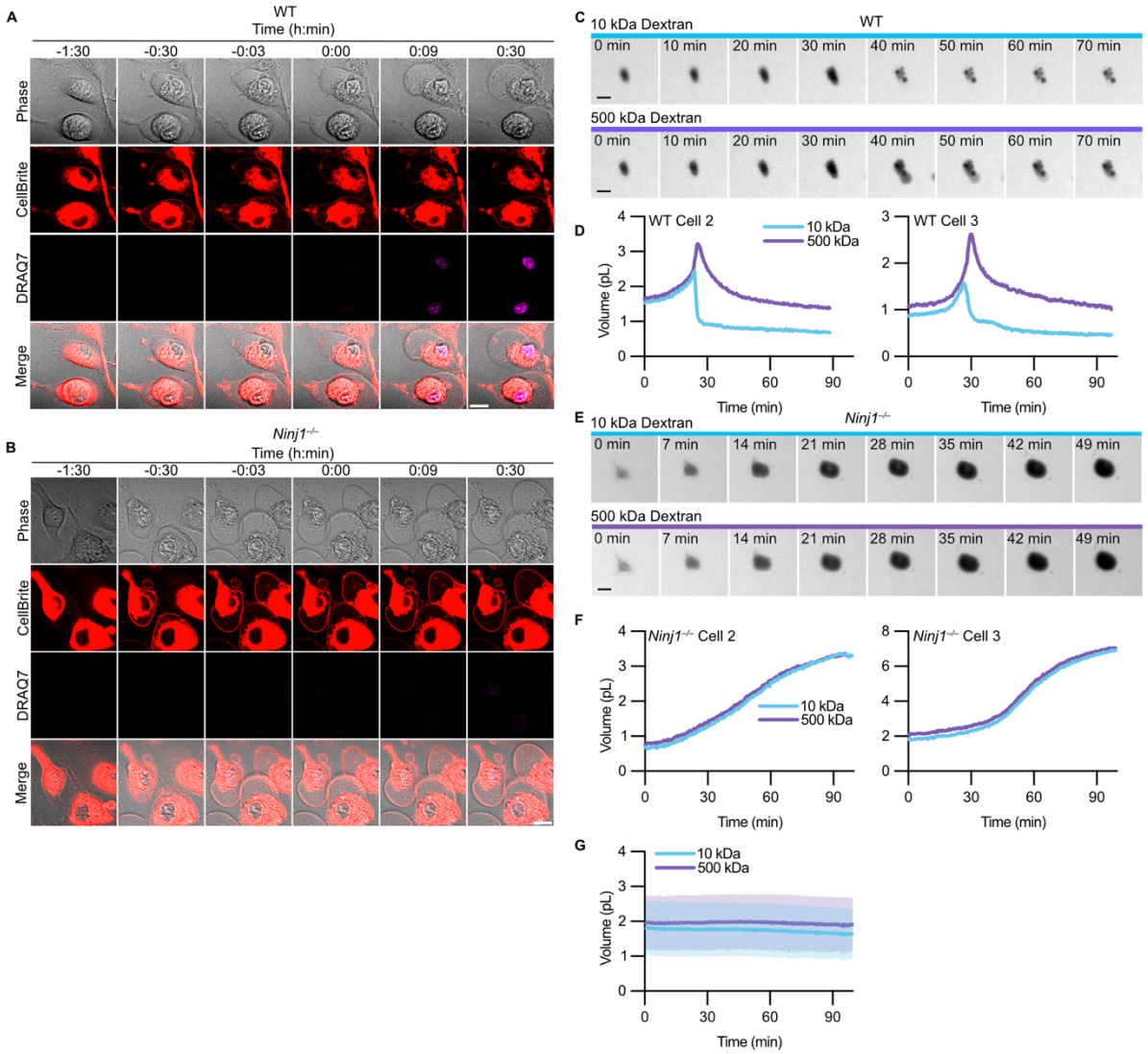

Figure S2 Cell swelling during ferroptosis is NINJ1-independent. A-B Stills from live cell imaging of WT (**A**) and *Ninj1*$^{-/-}$ (**B**) BMDMs stained with CellBrite and stimulated with ML162 in the presence of DRAQ7. Scale bar 10 µm. **C** Stills from FXm of WT iBMDMs treated with CuOOH. Scale bar 10 µm. **D** Volume measurements using FXm of WT iBMDMs treated with CuOOH in the presence of small (10 kDa Alexa647 Dextran) and large (500 kDa FITC Dextran) dyes. Time 0 indicates the onset of swelling. **E** Stills from FXm of *Ninj1*$^{-/-}$ iBMDMs treated with CuOOH. Scale bar 10 µm. Images in A representative of 3 independent experiments. Images in B and C are representative of cells from 2 independent experiments. **F** Volume measurements using FXm of *Ninj1*$^{-/-}$ iBMDMs treated with CuOOH in the presence of small (10 kDa Alexa647 Dextran) and large (500 kDa FITC Dextran) dyes. Time 0 indicates the onset of swelling. **G** Volume measurements using FXm of WT iBMDMs treated with ethanol in the presence of small (10 kDa Alexa647 Dextran) and large (500 kDa FITC Dextran) dyes. Time 0 indicates the first imaged frame. Images in A and B are representative of 3 independent experiments. Data in C and E are representative of 2 independent experiments. Each graph in D and F are values from one cell and are representative of at least 34 cells. Data in G are mean ± SD from 24 cells from 1 experiment.

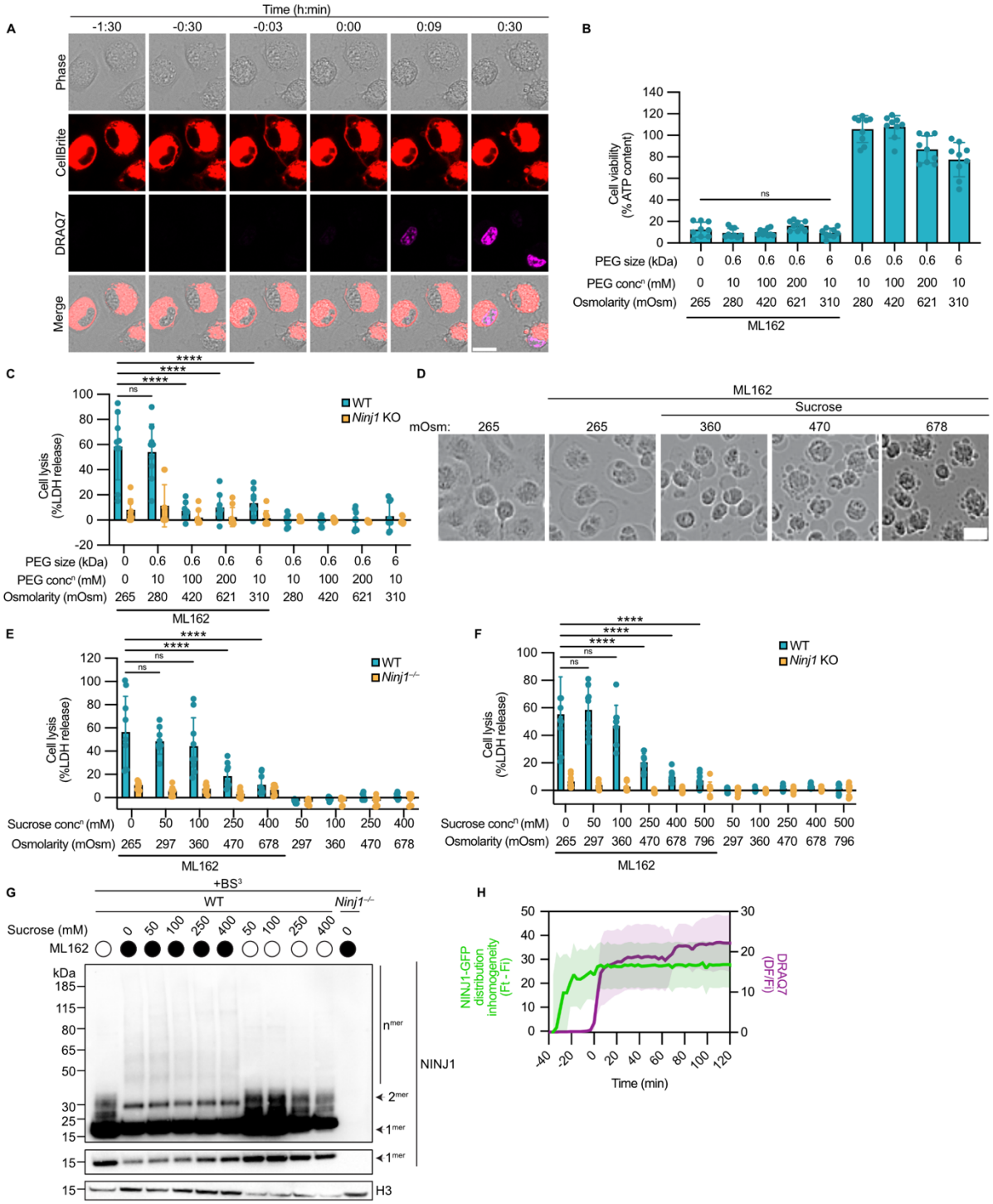

Figure S3 Osmoprotection prevents plasma membrane rupture in ferroptotic BMDMs and MEFs. A Stills from live cell imaging of WT BMDMs stimulated with ML162 stained with CellBrite in the presence of 10 mM PEG6000 and DRAQ7. Scale bar 10 µm **B** WT BMDMs were stimulated with ML162 in the presence of the indicated concentrations of PEG600 and PEG6000 for 4 h and their viability determined by measuring intracellular ATP. **C** WT and *Ninj1* KO MEFs were stimulated with ML162 in the presence of the indicated concentrations of PEG600 and PEG6000 and LDH release was analyzed after 7 h. **D** Phase contrast stills from Incucyte of WT BMDMs stimulated with ML162 in the presence of the indicated osmolarities of sucrose for 4 h. Scale bar 20 µm. **E** WT and *Ninj1*$^{-/-}$ BMDMs were stimulated with ML162 in the presence of the indicated concentrations of sucrose for 4 h and LDH release measured (**F**) WT and *Ninj1* KO MEFs were stimulated with ML162 in the presence of the indicated concentrations of sucrose for 7 h and LDH release measured (**G**) WT and *Ninj1*$^{-/-}$ BMDMs were stimulated with

ML162 in the presence of the indicated concentrations of sucrose for 4 h and NINJ1 oligomerization was probed by crosslinking Western blot. **H** Normalized quantification of the inhomogeneity distribution of NINJ1-GFP and DRAQ7 nuclear fluorescence intensity in HeLa cells after treatment with CuOOH. Data in B, C, E, F are mean ± SD from 3 independent experiments. Images in D and blot in G are representative of 3 independent experiments. Data in B, C, E and F were analyzed by 2-way ANOVA followed by Šídák's multiple comparisons tests, ns not significant, **** p<0.0001.

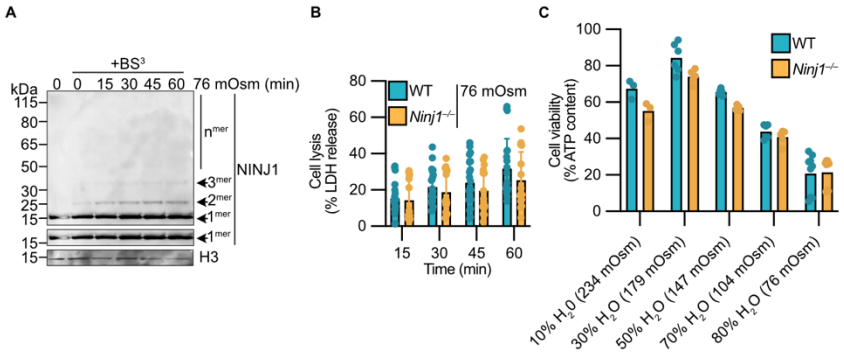

Figure S4 Hypotonic buffers lead to cell death. A-B BMDMs were incubated with 76 mOsm media for the indicated times and analyzed for NINJ1 oligomerization (**A**) and LDH release (**B**). **C** Viability of WT and *Ninj1*$^{-/-}$ BMDMs treated with the indicated osmolarities of media for 30 min was measured by quantifying intracellular ATP. Data in A is representative of 3 independent experiments. Data in B and C are from 3-6 independent experiments.

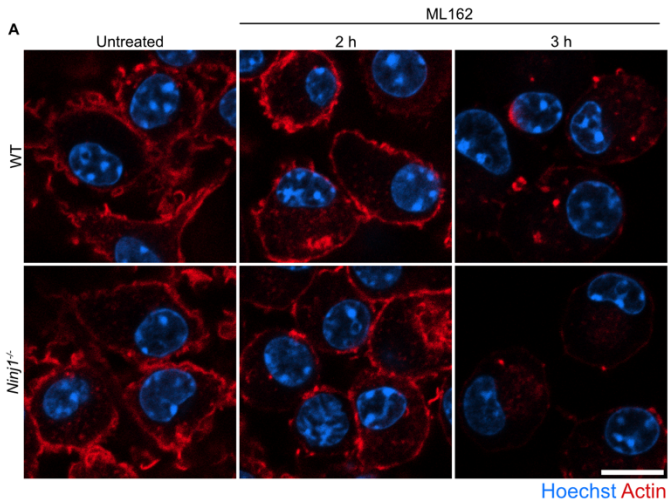

Figure S5 BMDMs lose cortical actin during ferroptosis. A Confocal micrographs of WT and *Ninj1*$^{-/-}$ BMDMs treated with ML162 and stained for filamentous actin. Scale bar 10 μm. Images are representative of 2 independent experiments.

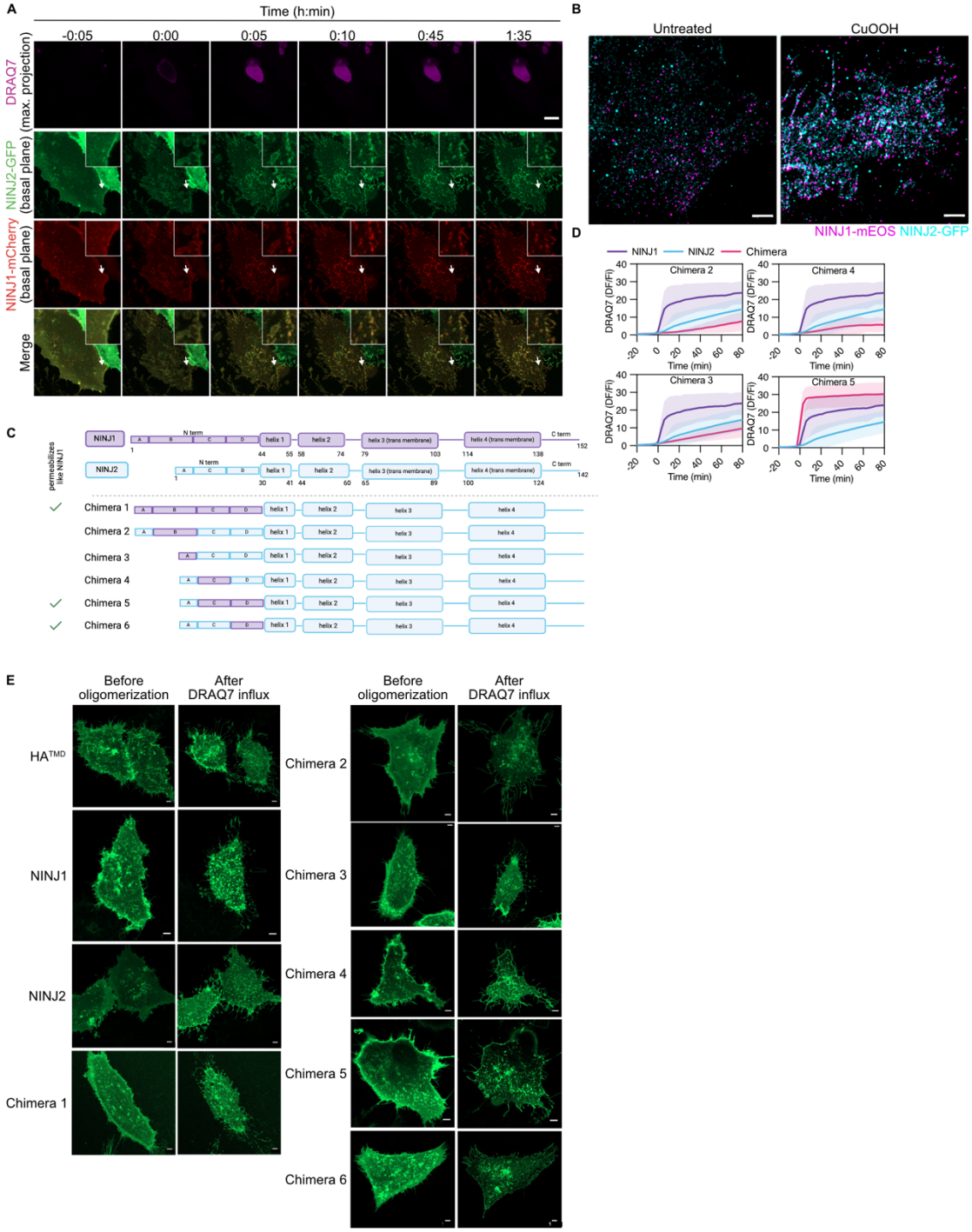

Figure S6 The N-terminus of NINJ1 endows NINJ2 with the ability to rupture the plasma membrane. A. Stills from live cell imaging of HeLa cells expressing NINJ1-mCherry and NINJ2-GFP in the presence of CuOOH and DRAQ7. Images show the NINJ1 and NINJ2 expression at the basal plane and the influx of DRAQ7 with a maximum intensity projection from a z-stack to track plasma membrane permeabilization. Time is normalized to the onset of the increase in DRAQ7. Scale bar 10 µm. **B.** STORM/PALM images of NINJ2-GFP and NINJ1-mEOS with or without CuOOH treatment. Scale bar 2 µm. **C.** Schematic of NINJ1/NINJ2 chimeras including full length proteins and the amino acid swaps that were performed. **D.** DRAQ7 intensity measured over time from maximum intensity projections. Live cell imaging performed on HeLa cells expressing the indicated construct were treated with CuOOH in the presence of DRAQ7. Time 0 indicates the first detectable DRAQ7 uptake. **E.** Stills from live cell imaging of indicated GFP-tagged constructs expressed in HeLa cells in the presence of CuOOH and DRAQ7. One still shortly after addition of CuOOH and prior to oligomerization is shown as well as a second after DRAQ7 influx and oligomerization. Data in A is representative of 3 independent experiments. Data in B is from two independent experiments. Data in D, E are mean ± SD from 3 independent experiments and 10-30 cells per condition.

Movie 1 WT BMDMs stained with CellBrite (Red) were treated with ML162 in the presence of DRAQ7 (Magenta) and imaged live with frames every 3 minutes. Movie is of a single Z slice.

Movie 2 *Ninj1*$^{-/-}$ BMDMs stained with CellBrite (Red) were treated with ML162 in the presence of DRAQ7 (Magenta) and imaged live with frames every 3 minutes. Movie is of a single Z slice.

Movie 3 WT BMDMs stained with CellBrite (Red) were treated with ML162 in the presence of 10 mM PEG6000 and DRAQ7 (Magenta) and imaged live with frames every 3 minutes. Movie is of a single Z slice.